Paleoceanography and Paleoclimatology®

RESEARCH ARTICLE

Key Points:

- The first high-resolution tropical sea surface temperature record shows that the Miocene Climatic Optimum was ~1.5°C warmer than the Early Miocene in the eastern equatorial Atlantic
- The West African Monsoon intensified following warming at ~17 Ma, resulting in variable surface ocean conditions forced by orbital cycles
- Intensification of the monsoon system caused increased dust supply and strong upwelling alternating with hyperstratification

Author Contributions:

Conceptualization: Evi Wubben
Data curation: Evi Wubben
Formal analysis: Evi Wubben, Bianca R. Spiering, Tjerk Veenstra, Remco Bos, Zongyi Wang, Isabella Raffi, Jakub Witkowski
Funding acquisition: Appy Sluijs
Investigation: Evi Wubben, Bianca R. Spiering
Methodology: Evi Wubben, Bianca R. Spiering

Tropical Warming and Intensification of the West African Monsoon During the Miocene Climatic Optimum

Evi Wubben[1] , Bianca R. Spiering[1] , Tjerk Veenstra[1], Remco Bos[1], Zongyi Wang[1], Joost van Dijk[1], Isabella Raffi[2], Jakub Witkowski[3], Frederik J. Hilgen[1], Francien Peterse[1] , Francesca Sangiorgi[1] , and Appy Sluijs[1]

[1]Department of Earth Sciences, Faculty of Geosciences, Utrecht University, Utrecht, The Netherlands, [2]International Research School of Planetary Sciences (IRSPS), Università degli Studi 'G. d'Annunzio' di Chieti, Pescara, Italy, [3]Institute of Marine and Environmental Sciences, University of Szczecin, Szczecin, Poland

Abstract Studying monsoon dynamics during past warm time periods such as the Miocene Climatic Optimum (MCO; ~16.9–14.5 Ma) could greatly aid in better projecting monsoon intensity, in the context of future greenhouse warming. However, studies on regional MCO temperature change and its effect on the monsoons during this time period are lacking. Here, we present the first high-resolution, low-latitude record of sea surface temperature (SST) and paleoceanographic change covering the Miocene Climatic Optimum, in the eastern equatorial Atlantic, at Ocean Drilling Program Site 959, based on TEX$_{86}$ paleothermometry. SSTs were ~1.5°C warmer at the onset of the MCO (16.9 Ma) relative to the pre-MCO (~18.3–17.7 Ma). This warming was accompanied by a transient increase in %total organic carbon. Prior to the MCO, sediment composition, geochemical proxy data as well as dinoflagellate cyst assemblages imply a productive surface ocean at Site 959. Immediately following the MCO onset (~16.9–16.5 Ma), we record an intensification of the West African Monsoon (WAM) characterized by higher amplitude variability in all proxy records on precession to obliquity timescales. We interpret increased orbital-scale SST, biogenic Ba and dinocyst assemblage variability to represent intensification of equatorial upwelling, forced by the WAM strength. Furthermore, higher SSTs during eccentricity maxima correlate to increased relative abundances of the warm and stratification-favoring dinocyst *Polysphaeridium zoharyi*, during periods of low WAM intensity. Finally, while long-term SSTs decline toward the middle Miocene, maximum SSTs and *Polysphaeridium zoharyi* abundances occur during MCO peak warming at ~15.6 Ma.

Plain Language Summary The global climate during the Miocene Climatic Optimum (MCO) (~16.9–14.5 Ma) was warm, perhaps similar to the future. Better understanding the climate system during this time period could aid in predicting future climate change. Tropical climates are the engine of global climate because they transport heat and moisture to higher latitudes with winds and ocean currents. Monsoons are an important feature of tropical climates. Importantly, continuous sea surface temperature reconstructions covering the MCO from the tropics are lacking. Here, we present an unprecedented resolution novel sea surface temperature record using sediments recovered in the eastern equatorial Atlantic Ocean which cover the MCO. Surface ocean temperatures rose by ~1.5°C between the Early Miocene (~18.3–17.7 Ma) and the onset of the MCO. Concomitantly, we record an increase in wind strength, surface ocean mixing and biological growth in the ocean, caused by a stronger West African Monsoon in this warmer climate. The monsoon strength is also strongly determined by variations in solar insolation, through periodic variations in the Earth's orbit. The recorded monsoon intensification with warming is consistent with projections of future monsoons under modern global warming.

1. Introduction

The Early to Middle Miocene stands out in Cenozoic climate and carbon cycle records because of the Miocene Climatic Optimum (MCO; ~16.9–14.5 Ma). Deep ocean benthic foraminifer oxygen isotope ratios (δ^{18}O) define the MCO with an abrupt ~1‰ negative excursion at ~16.9 Ma (Holbourn et al., 2007, 2015; Woodruff & Savin, 1991). Stable carbon isotope ratios (δ^{13}C) show ~0.8‰ positive excursion at ~16.7 lasting approximately 3.4 Myr, termed the Monterey Excursion (ME; Diester-Haass et al., 2009; Holbourn et al., 2007, 2015; Sosdian & Lear, 2020; Vincent & Berger, 1985). Temperature reconstructions indicate that the MCO was on average ~7–8°C warmer than today (Herbert et al., 2020; Steinthorsdottir, Coxall, et al., 2021 and references therein) and

Supervision: Frederik J. Hilgen, Francien Peterse, Francesca Sangiorgi, Appy Sluijs
Validation: Evi Wubben, Bianca R. Spiering
Visualization: Evi Wubben
Writing – original draft: Evi Wubben
Writing – review & editing: Evi Wubben, Bianca R. Spiering, Isabella Raffi, Jakub Witkowski, Frederik J. Hilgen, Francien Peterse, Francesca Sangiorgi, Appy Sluijs

atmospheric pCO_2 reached values between ∼400–600 ppm, with transient peaks of 800 ppm (Cui et al., 2020; Ji et al., 2018; Sosdian et al., 2018; Steinthorsdottir, Jardine, & Rember, 2021; Stoll et al., 2019; Super et al., 2018). Such temperature and pCO_2 levels are broadly in line with projected future climate trends, particularly similar to the middle range of predictions (i.e., RCP 4.5 to RCP 6.0), subjected to climate sensitivity and emission scenarios (Collins et al., 2013). During the Early to Middle Miocene, the continental configuration and vegetation patterns transitioned to conditions similar to today. Continental ice sheets were present on Antarctica, although much reduced during the MCO, a state referred to as a unipolar Coolhouse climate (Liebrand et al., 2017; Miller et al., 2020; Westerhold et al., 2020). Hence, the MCO presents an interesting "intermediate deep-time climate analogue" to study past changing climate systems in the context of future greenhouse warming (Burke et al., 2018; Steinthorsdottir, Coxall, et al., 2021).

During the onset of the MCO (∼16.9 Ma), the deep ocean benthic foraminifer $\delta^{18}O$ excursion marks a possibly global abrupt warming phase, but reconstructions of absolute temperature trends at the Earth surface are sparse. In the western North Atlantic, a >5°C warming is recorded just prior to the onset of the MCO (∼19–18 Ma; Guitián et al., 2019). Across the MCO, multi-proxy reconstructions show values of up to ∼15°C higher than present day (∼30–35°C) in the middle-to high-latitude North Atlantic Ocean and Danish North Sea (Herbert et al., 2020; Super et al., 2018, 2020). During the MCO, TEX_{86}-based paleotemperatures from the eastern mid-latitude North Atlantic show maximum temperatures up to ∼27°C (Sangiorgi et al., 2021). In the Southern Ocean, reliable temperature estimates covering the onset of the MCO are limited due to frequent hiatuses in recovered sections (Hartman et al., 2018; Sangiorgi et al., 2018). However, ocean temperatures as high as ∼15°C have been reconstructed from offshore Wilkes Land (East Antarctica; Sangiorgi et al., 2018) and temperatures of ∼7°C were recorded at an ice-proximal site in the western Ross Sea (Levy et al., 2016). Unfortunately, the reliability of reconstructed absolute temperatures strongly depends on the selection of calibration models and biomarker production depth (e.g., lipid biomarker proxy TEX_{86}), proxy saturation and associated calibration limits (e.g., lipid biomarker proxy $U^{k'}_{37}$), and potential bias by non-thermal effects such as considerable input of terrestrial organic matter and local effects such as meltwater pulses at ice-proximal sites. Recently, combined proxy SST reconstructions, including lipid biomarkers and clumped isotope paleothermometry, from the South Tasman Rise and offshore Northwest Australia show temperatures that are much higher than the present day ones during the MCO (Leutert et al., 2020; Modestou et al., 2020). Collectively, even though relatively high temperatures during the MCO are recorded at multiple sites, an abrupt warming at the onset of the MCO, as suggested by the deep ocean $\delta^{18}O$ record is not apparent in most of these surface records.

Crucially, high-resolution, low-latitude (tropical) SST records covering the onset of the MCO are scarce (Steinthorsdottir, Coxall, et al., 2021). This lack of low-latitude SST records is surprising given that tropical climate variability is decisive for atmospheric circulation by governing the intensity of trade winds and thereby monsoonal precipitation and weathering (Adegbie et al., 2003; Dupont et al., 1998; Steinthorsdottir, Coxall, et al., 2021). This can drive extratropical warming by both marine and atmospheric teleconnections and subsequently play a key part in global climate variability. In addition, tropical temperature variability might drive carbon cycle feedbacks related to organic matter burial and the $\delta^{13}C$ of the global exogenic carbon pool (Berner, 1982; Berner et al., 1983; Hedges & Keil, 1995), modulated by variations in regional insolation through Milankovitch cycles. During the Early to Middle Miocene, this Milankovitch forcing is reflected in strong eccentricity cycles in benthic foraminifer $\delta^{13}C$ records, termed Carbon Maxima (CM) events (Holbourn et al., 2015; Kocken et al., 2019; Ma et al., 2011; Woodruff & Savin, 1991). Previously, the focus has been on reconstructing equatorial Pacific temperature variability during the Middle Miocene to evaluate responses of the eastern Pacific cold tongue and western Pacific warm pool (Fox et al., 2021; Rousselle et al., 2013; Sosdian & Lear, 2020). Reconstructions of tropical Atlantic Ocean SSTs rely only on low resolution (>100 kyr) reconstructions from Ceara Rise in the western equatorial Atlantic (Sosdian et al., 2018; Z. Zhang et al., 2013). Overall, we lack records from tropical latitudes across the Early and Middle Miocene to assess whether the MCO was associated with tropical warming, on a resolution sufficient to quantify orbital scale variability in relation to monsoons.

Recently, an orbitally tuned age model was constructed for sediments recovered at Ocean Drilling Program (ODP) Site 959 in the eastern equatorial Atlantic (Spiering et al., 2024; Wubben et al., 2023). This showed the presence of a stratigraphically extensive Early to Middle Miocene (∼18.5–15.0 Ma) section, albeit with a ∼700 kyr hiatus prior to the onset of the MCO. Importantly, previously generated lithological and geochemical records of the Miocene sequence at Site 959 suggest considerable influence of orbital cyclicity (eccentricity,

obliquity and precession) likely related to West African Monsoon (WAM)-induced atmospheric circulation (Norris, 1998; Vallé et al., 2017; Wagner, 2002; Wubben et al., 2023), which is assessed in detail in a companion paper (Spiering et al., 2024). The WAM is crucial for regulating the low-latitude, atmospheric moisture- and heat budget and, at present, represents a key factor in regulating rain-fed agriculture in densely populated western Sub-Saharan Africa. This region, where agricultural production is directly dependent on rainfall, is particularly sensitive due to its limited resources for adaptation to impacts by climate change (Camberlin et al., 2001; Challinor et al., 2007). The African monsoon is projected to be amplified as a result of modern global warming (Masson-Delmotte et al., 2021). Specifically, simulations predict a larger global monsoon area and both increased and intensified precipitation, due to higher atmospheric humidity by increased evaporation, changing specific sea-air moisture content and moisture convergence (Hsu et al., 2013; Seth et al., 2019). To further elucidate the response of WAM circulation on climatic warming, the MCO can form a potential analog to evaluate the response of the paleo-WAM to climatic warming similar to today.

Previous studies have focused on African monsoon dynamics from a Mediterranean perspective, reflecting North African monsoonal hydrology (Bosmans, Drijfhout, et al., 2015; Marzocchi et al., 2015), also during the MCO (Zammit et al., 2022), but the WAM system is largely underexplored. Major element intensities have shown that Late Miocene to Early Pleistocene marine sedimentation at Site 959 was paced by eccentricity, obliquity, and precession cycles, recording variable continental run-off, dust fluxes, and upwelling, sensitive to high-latitude ice volume changes (Norris, 1998; Vallé et al., 2017). However, it remains questionable whether a much-reduced Antarctic Ice Sheet (Miller et al., 2020) could have considerably influenced African monsoon intensity. A low-resolution evaluation of dinocyst assemblages from Late Eocene to Middle Miocene sediments at Site 959 revealed strikingly variable abundances of genera indicative of upwelling zones or a stratified water column in the Early to Middle Miocene (Awad & Oboh-Ikuenobe, 2019; Oboh-Ikuenobe et al., 1999). Furthermore, model simulations (CESM 1.2) of WAM evolution during the Middle Miocene (14 Ma) yield a weakening monsoon system highly sensitive to paleo-location of the West African coast as well as atmospheric CO_2 forcing (Acosta et al., 2022). More particularly, a progressively more northern position of the African continent shifted monsoon circulation to the subtropics during the Miocene, which weakened circulation and increased seasonality (Acosta et al., 2022). However, the influence of changing orbital configurations has not been tested, and uncertainty in the adoption of paleogeography models and vegetation patterns remain (Acosta et al., 2022).

Here, we present TEX_{86} (TetraEther Index of tetraethers with 86 carbon atoms; Schouten et al., 2002, 2013) - based seawater temperatures and organic dinoflagellate cyst (dinocyst) assemblages across the onset of the MCO at Site 959 (~18.3–15.0 Ma) and combine these records with previously published lithological and geochemical data from the same samples (Spiering et al., 2024; Wubben et al., 2023). Our high-resolution sampling provides an unprecedented evaluation of surface water conditions during the MCO and allows us to assess (a) warming in the tropics during the MCO, and (b) the effect of tropical warming on WAM circulation by tracing variability in processes such as (export) productivity, upwelling and dust supply on precession to eccentricity timescales.

2. Materials and Oceanographical and Geological Setting

2.1. ODP Site 959

The ODP Site 959 sedimentary sequence was recovered during Leg 159 in the eastern equatorial Atlantic Ocean, ~120 km offshore Ivory Coast on the southern edge of the Deep Ivorian Basin (3°37.659′N, 2°44.112′W; Figure 1; Mascle et al., 1996). The site was located at ~1°S (±2.5°, using the paleomagnetic reference frame of Torsvik et al. (2012)) during the Early to Middle Miocene (paleolatitude.org version 2.1; van Hinsbergen et al., 2015). Lower and Middle Miocene sediments were recovered in Hole 959A, retrieved at ~2,100 m water depth on a platform north of the Côte d'Ivoire-Ghana Marginal Ridge (Mascle et al., 1996). Following Vallé et al. (2017) and van der Weijst et al. (2022), we use the depth scale introduced in Wubben et al. (2023) in which constant offsets of 0.5 m are added to each core to correct for sediment loss between cores. Consequently, the studied cores 28× to 21× span the depth interval between 280.02 and 207.99 rmbsf (see Supplementary Information T1 in Wubben et al. (2023)). The detailed age model, which was constructed based on calcareous nannofossil and diatom biostratigraphy combined with orbital tuning of the bulk carbonate $\delta^{13}C$ record, implies that the sediment cores (28X-1W 74 cm–21X-1W 23 cm) span the interval from ~18.3 to 15 Ma, including a hiatus between ~17.6 and 17.0 Ma (Spiering et al., 2024; Wubben et al., 2023).
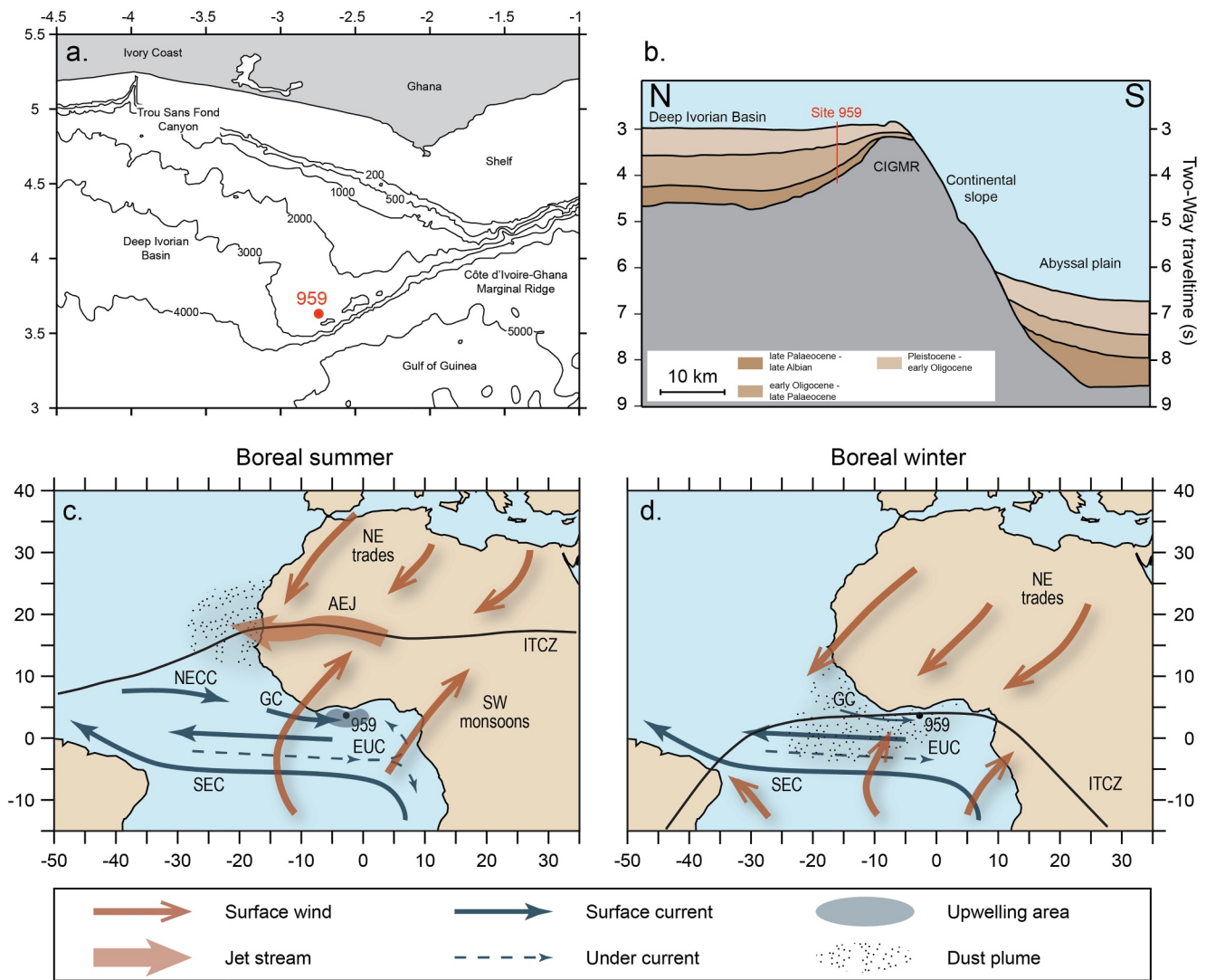
Figure 1. (a) Bathymetric map with location of Ocean Drilling Program Site 959. Lines and numbers represent bathymetry taken from Basile et al. (1998), map modified from Spiering et al. (2024). (b) North-South cross section of Site 959 coring location on the Côte d'Ivoire-Ghana Marginal Ridge (CIGMR), based on multichannel seismic profiles from Mascle et al. (1996). (c, d) Map of the equatorial Atlantic Ocean showing the main modern West African Monsoon wind- and ocean circulation patterns during boreal summer (c) and boreal winter (d). Both maps are modified from Spiering et al. (2024).

Sediments mostly comprise marine biogenic components, notably (diagenetically altered) biogenic opal and calcareous nannofossils, with some clay and organic matter (Mascle et al., 1996; Wagner, 2002). Lithological variability is characterized by decimeter-to-meter scale variations in diatom nannofossil chalk and clayey diatomite (Subunit IIA; 29X-CC–23X-4W, 40 cm) in the Lower Miocene, which progressively grade into alternating nannofossil chalk and clay in the Middle Miocene (Subunit IB; 23X-4W–21X, 40 cm) (Mascle et al., 1996). We refer to Mascle et al. (1996) and Wubben et al. (2023) for detailed lithological descriptions.

Bulk carbonate $\delta^{18}O$ and $\delta^{13}C$ at Site 959 imply the presence of the onset of the MCO at ~258 rmbsf (~16.9 Ma), the Monterey Excursion (ME) between ~250 and 225 rmbsf, including Carbon Maxima (CM) events 1 to 4 (~16.8–15.2 Ma), and peak warming at ~221.19 rmbsf (~15.6 Ma; Wubben et al., 2023) (Figure 2). Records of magnetic susceptibility (MS), mean greyscale (GS) and estimated weight percent (wt%) $CaCO_3$ at on average <5 kyr resolution imply a dynamic depositional setting across the MCO at Site 959 (Wubben et al., 2023). Prior to the MCO onset (~18.2–17.7 Ma), intervals of increased productivity, characterized by dark, diatomaceous sedimentation and low wt% $CaCO_3$ occur during eccentricity maxima (Wubben et al., 2023). It is hypothesized that these intervals are related to episodes of increased upwelling of nutrient-rich waters, supported by enrichment
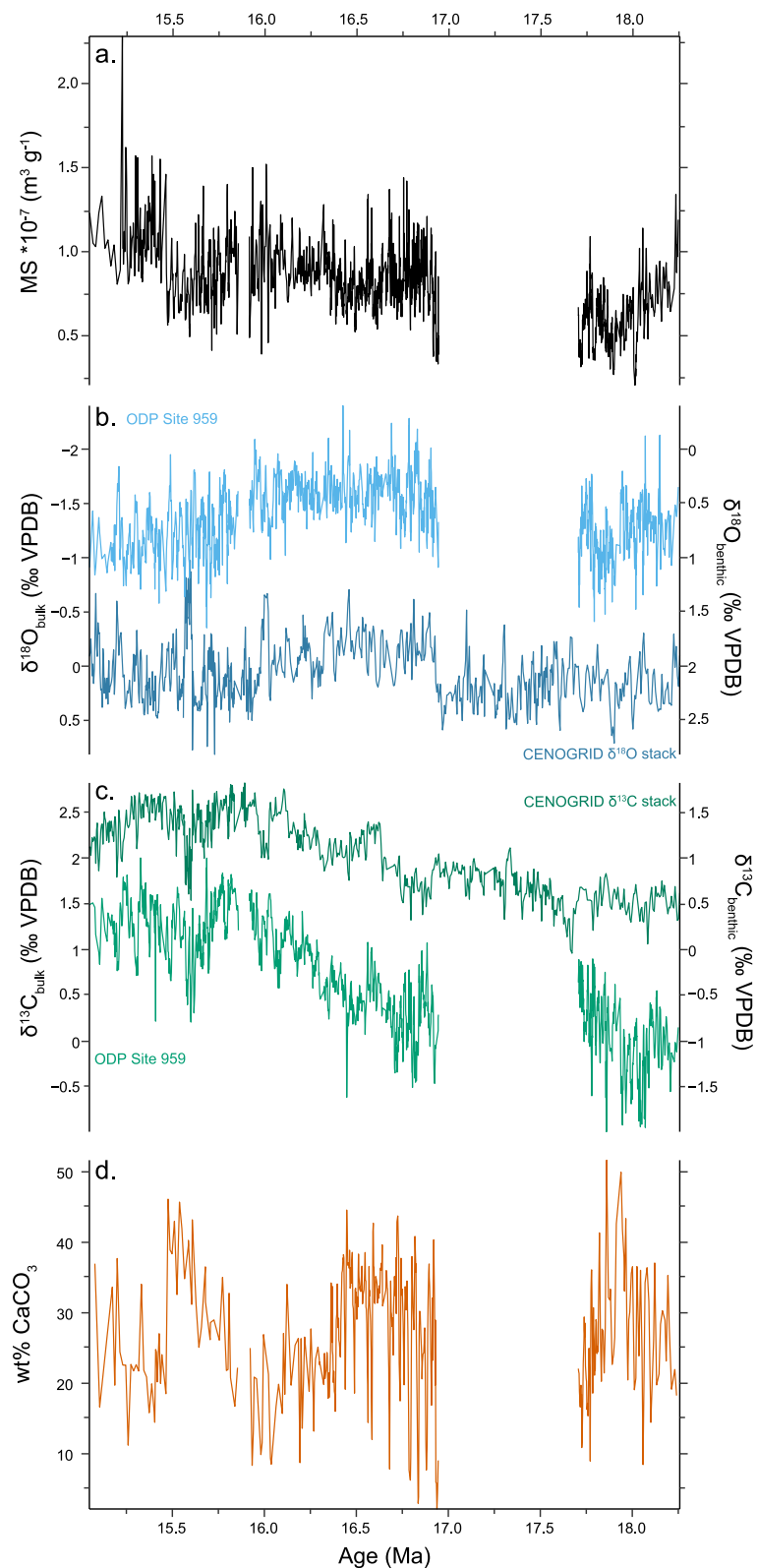
Figure 2. Compilation of geochemical proxy records from Ocean Drilling Program Site 959 prior to and during the Miocene Climatic Optimum, previously generated by Wubben et al. (2023), compared to benthic foraminifer isotope trends (Holbourn et al., 2015; Westerhold et al., 2020). (a) Magnetic susceptibility. (b) Site 959 bulk carbonate $\delta^{18}O$ (light blue) and benthic foraminifer $\delta^{18}O$ from the eastern equatorial Pacific (dark blue). (c) Site 959 bulk carbonate $\delta^{13}C$ (light green) and benthic foraminifer $\delta^{13}C$ from the eastern equatorial Pacific (dark green). (d) Weight percentage (wt%) of $CaCO_3$.

of biogenic Ba (Spiering et al., 2024; Wubben et al., 2023). Toward the Middle Miocene, production potentially shifted to dominantly carbonate producers and lithology mainly alternates between clays and carbonates. Strikingly, immediately following the onset of the MCO (~16.9–16.3 Ma), high-amplitude alternations between diatomite and carbonate-rich deposits on precession to obliquity timescales coincide with a node in the long, ~2.4 Myr-long eccentricity cycle (Spiering et al., 2024; Wubben et al., 2023).

2.2. Regional Oceanography and the West African Monsoon

Modern SST at Site 959 range from ~25.0 to 28.5°C (Locarnini et al., 2013). Surface ocean circulation in the eastern equatorial Atlantic is governed by two principal currents, that is, the westward-flowing North Equatorial Current (NEC) and the South Equatorial Current (SEC), of which the latter facilitates the flow of warm waters toward the South American continent (Brazil margin; Norris, 1998). During boreal summer, the Intertropical Convergence Zone (ITCZ) is displaced northward, which facilitates an intensified North Equatorial Counter-current (NECC) that extends into the eastward-flowing Guinea Current (GC) that flows into the Guinea Basin. Simultaneously, the eastward-flowing Equatorial Undercurrent (EUC) transports cool and saline waters to the Guinea Basin in the subsurface which results in a strong thermocline relative to the warm, low-salinity GC (Norris, 1998; Verstraete, 1992). The EUC strengthens during boreal summer due to strong trade winds over the western and central low-latitude Atlantic that cause increased pile-up of warm surface waters to the Brazil margin. This results in a stronger eastward-flowing subsurface current (i.e., the EUC) that withstands westward-flowing surface currents (Norris, 1998; Verstraete, 1992). Consequently, a stronger EUC transports cooler sub-surface waters into the eastern equatorial Atlantic and the Gulf of Guinea (GG) which produces seasonal upwelling along the west African coast (Figure 1c) (Djakouré et al., 2017; Norris, 1998; Verstraete, 1992; Wagner, 1998). Conversely, the EUC and GC are relatively weak during boreal winter, when the ITCZ is in its southernmost position and westward surface winds prevent a strong NECC (Norris, 1998) (Figure 1d).

Sedimentation in the eastern equatorial Atlantic, and thereby at ODP Site 959 is influenced by WAM variability. The WAM system reflects extreme seasonal migrations of the ITCZ relative to the equator associated with strong differential seasonal heating between North Africa and the ocean, effectively changing the position of trade wind conversion over Africa (Gadgil, 2018 and references therein). Monsoon precipitation over West Africa is the strongest during (eccentricity-modulated) precession minima, that is, maximum boreal summer heating. Strong monsoons also occur during obliquity maxima, when increased Northern Hemisphere (NH; boreal) solar radiation enforces increased seasonality and thereby increased land-ocean temperature gradients (Bosmans, Drijfhout, et al., 2015; Bosmans, Hilgen, et al., 2015; Marzocchi et al., 2015; Tjallingii et al., 2008; Weldeab et al., 2007). During precession minima and a northward shift of the ITCZ (~18°N) directly related to intensified ascending branch of the Hadley cells, precipitation increases over North Africa (Bosmans, Drijfhout, et al., 2015; deMenocal et al., 1993; Kutzbach et al., 2014; Larrasoaña et al., 2013; Marzocchi et al., 2015; Trauth et al., 2009). During precession maxima, precipitation is increased over the Atlantic. Increased dust supply to the eastern equatorial Atlantic and GG occurs when summer insolation minima during precession maxima, modulated by eccentricity, result in a weakened monsoon and a more arid African continent (Larrasoaña et al., 2003; Norris, 1998; Tiedemann et al., 1994; Trauth et al., 2009). Dust fluxes to Site 959 are forced by intensified NE trade winds (i.e., Harmattan) which transport dust sourced from the Sahel region (Norris, 1998; Trauth et al., 2009; Vallé et al., 2017). Model simulations on sub-precession timescales show a bimodal (April–May & September–October) precipitation response over the equatorial West African region while surface air temperatures remain relatively low (~28°C) because of increased cloud cover (Marzocchi et al., 2015).

3. Methods

3.1. Bulk Total Organic Carbon

To determine the percentage of bulk total organic carbon (%TOC) approximately 1 g of selected freeze-dried samples ($n = 145$) were powdered and transferred to 50 ml Greiner tubes. To remove carbonates, the samples were treated twice with 25 ml of 1 M HCl and in between decarbonation they were shaken, centrifuged, and rinsed with UHQ. After drying in the oven for at least 72 hr at 60°C, approximately 30 mg of the decalcified, homogenized residues was used to measure %TOC with a Fisons CNS analyzer at Utrecht University. A standard (GQ) was repeatedly measured in each run to determine precision (1σ: 0.04%).

3.2. GDGT Analysis and TEX$_{86}$ Paleothermometry

Approximately 5 g of 568 sediment samples at an average resolution of ∼10 cm between ∼18.2 and 15.0 Ma were selected for the generation of a TEX$_{86}$ paleotemperature record based on glycerol dialkyl glycerol tetraether (GDGT) lipids. Lipid extraction from freeze-dried, powdered samples was carried out using either Dionex accelerated solvent extraction (ASE 350) or microwave extraction (MEX) and using 9:1 (v:v) dichloromethane (DCM):MeOH. A known amount of synthetic C$_{46}$ glycerol trialkyl glycerol tetraether (m/z 744) internal standard was added to the obtained total lipid extract (TLE) and evaporated to near dryness under a gentle N$_2$ flow. The TLEs were passed over a small Na$_2$SO$_4$ column to remove residual water and sediment using DCM, and, after drying under N$_2$, separated into three fractions according to polarity, that is, apolar, neutral and polar fractions, using Al$_2$O$_3$ column chromatography and hexane:DCM (9:1), hexane:DCM (1:1) and DCM:MeOH (1:1) as eluents, respectively. Subsequently, the polar fractions, containing the GDGTs, were dissolved in hexane:iso-propanol (99:1) solution to a concentration of ∼2 mg/ml, and passed over a 0.45 μm polytetrafluoroethylene (PTFE) filter prior to injection on an Agilent 1260 Infinity series high performance liquid chromatograph (HPLC), coupled to an Agilent 6130 single-quadrupole mass spectrometer (MS) with instrument settings and methodology of Hopmans et al. (2016). The GDGTs were detected by their [M+H]$^+$ ions where a minimum peak area of 3,000 and a signal-to-noise ratio >3 was maintained as threshold for quantification. GDGT abundance was determined by comparison of their peak area with that of the internal standard, and assuming a similar response of the mass spectrometer for all compounds.

Seawater temperatures were reconstructed by applying the TEX$_{86}$ paleothermometer. The TEX$_{86}$ is based on the temperature-dependent cyclization in isoprenoid GDGTs (isoGDGT), which are membrane lipids of Thau-marchaeota (Schouten et al., 2002). The TEX$_{86}$ determines the relative abundance of four different isoGDGTs that is, GDGT-1,-2,-3 and crenarchaeol isomer (cren') (1), in which GDGT-n represents the number (n) of cyclopentane rings on its hydrocarbon chains. The crenarchaeol isomer contains four cyclopentane as well as one cyclohexane rings.

$$
TEX_{86} = \frac{\left([GDGT-2] + [GDGT-3] + \left[cren'\right]\right)}{\left([GDGT-1] + [GDGT-2] + [GDGT-3] + \left[cren'\right]\right)}
\tag{1}
$$

To test for factors other than temperature that could potentially influence TEX$_{86}$, we evaluated several indices to check for possible deviation from modern analogs, such as the weighted average of cyclopentane moieties (Ring Index; Zhang et al., 2016), contributions of isoGDGT produced by methanotrophic or methanogenic archaea (Methane Index; Zhang et al. (2011), GDGT-2/Crenarchaeol; Weijers et al. (2011), and GDGT-0/Crenarchaeol ratio; Blaga et al. (2009), respectively) and contributions by deep-dwelling archeal communities (GDGT-2/GDGT-3 ratio; Taylor et al., 2013) (see Supporting Information S1). Furthermore, the astronomically tuned age model presented for the Early to Middle Miocene record at Site 959 allows us to determine absolute accumulation rates (AR) of GDGT compounds on kyr-timescales (ng GDGT cm^{-2} kyr^{-1}). Therefore, next to evaluating the branched and isoprenoid tetraether (BIT) index that quantifies the relative input of soil-derived GDGTs to marine sediments (Hopmans et al., 2004; Weijers et al., 2006), we also determine the isoGDGT and branched GDGT (brGDGT) ARs. IsoGDGT- and brGDGT ARs are normalized to TOC to correct for changes in AR induced by variability in productivity.

Multiple studies have calibrated TEX$_{86}$ to mean annual SST based on modern marine core-top sediments, using linear (O'Brien et al., 2017; Schouten et al., 2002; Tierney & Tingley, 2014) and non-linear (Kim et al., 2010; Liu et al., 2009) regression models. These models differ particularly at the high temperature end, which is likely relevant for the MCO at a tropical location such as Site 959 in case that TEX$_{86}$ exceeds values found for the modern ocean (up to 0.73) and the TEX$_{86}$-SST relationship needs to be extrapolated. In addition, recent work has indicated that most of the sedimentary isoGDGT pool is not produced at the surface, but in the shallow subsurface, that is, between ∼50–200 m, supporting shallow subsurface calibrations (Ho & Laepple, 2015; Kim et al., 2010; Schouten et al., 2002; Tierney & Tingley, 2014). Moreover, deeper dwelling GDGT-producers, characterized by high GDGT-2/GDGT-3 values, may contribute to the TEX$_{86}$ signal stored in the sediments (Hurley et al., 2018; Rattanasriampaipong et al., 2022; Taylor et al., 2013; van der Weijst et al., 2022). Unfortunately, a proper calibration for the "right" and dynamical depth range is not yet available. Therefore, to account for this

uncertainty, by convention (Hollis et al., 2019), TEX_{86} will here be translated into temperature using both the logarithmic calibration model (Kim et al., 2010; TEX_{86}^{H}) (2) and a linear calibration model (O'Brien et al., 2017; $TEX_{86-Linear}$) (3) (Figure S2 in Supporting Information S1):

$$TEX_{86}^{H} \quad SST = 68.4 \times \log(TEX_{86}) + 38.6 \tag{2}$$

$$TEX_{86-Linear} \quad SST = 0.017 \times TEX_{86} + 0.19 \tag{3}$$

We consider it likely that the relatively sensitive linear SST calibration overestimates the variability at the high temperature-end (Cramwinckel et al., 2018; Ho & Laepple, 2016), and that an exponential calibration may better reflect temperature variability in this range. Therefore, we use the exponential TEX_{86}^{H} calibration to discuss the temperature variability at Site 959 in Section 5. In addition, we explore an exponential model that is calibrated to shallow subsurface (100–250 m water depth) temperatures (Ho & Laepple, 2016, $SubT_{100-250m}$) (4). Any calibration based on seawater temperatures below the mixed layer will lead to a lower proxy sensitivity than one based on mixed layer temperatures due to a smaller global temperature range in subsurface waters (Ho & Laepple, 2016). Because shallow subsurface temperature variability typically reflects that at the sea surface (Ho & Laepple, 2015), we here assume that this record is a suitable, conservative reflection of SST variability at our site (Figure S2 in Supporting Information S1).

$$SubT_{100-250m} \quad SubT = 45.91 \, (\pm 1.55) \times \log(TEX_{86}) + 25.6 (\pm 0.42) \tag{4}$$

3.3. Palynology

3.3.1. Lab Processing and Quantification

About 10–15 g of 90 freeze-dried samples between ~18.2–15.0 Ma (Cores 27X-7, 39 cm–21X-2, 102 cm) were coarsely crushed and the sediment was processed for palynology at Utrecht University. We chose the highest resolution between ~15.75–15.65 Ma (±4.4 kyr; Cores 22X-5, 103 cm–22X-4, 17 cm) and between ~17.0–16.75 Ma (±10 kyr; Cores 25X-CC–25X-3, 50 cm), and an average resolution of ±35 kyr in the remaining parts of the record. A tablet containing a known number of *Lycopodium clavatum* spores was added to each sample to enable determination of dinocyst absolute abundances (dinocyst/gram dry sediment) followed by standard palynological treatment (e.g., Brinkhuis et al., 2003). Subsequently, in a 40 ml plastic vial, each sample was treated with 10% hydrochloric acid (HCl) to remove carbonates. After settling overnight, the vials were centrifuged, subsequently decanted, and filled up with deionized water. After decanting, 40% cold hydrofluoric acid (HF) was added to remove silicates, and samples were subsequently put on a shaking machine for 2 hr. After settlement overnight the samples were again treated with HCl and HF. No oxidation was carried out. Finally, the samples were decanted and rinsed with demineralized water. Residues were washed over a 10 μm mesh-sized sieve and briefly put in an ultrasonic bath to break-up aggregates of organic matter and remove remaining minerals such as pyrite. For each sample, two slides were prepared using glycerin and sealed with varnish.

Where possible, up to a minimum of 200 organic walled dinocysts were counted per sample at 400× and 630× magnification using a Leica DMLB microscope connected to a Leica MC120 HD camera. For six samples, microscopic slides yielded less than 100 specimens, and these were not considered in statistical analyses. Dinocyst identification follows the taxonomy of Williams et al. (2017) and, where preservation and cyst size were sufficient to identify characteristic features, dinocysts were quantified one the species level. A consistency check between counts carried out by multiple analysts was performed. Terrestrial palynomorphs (pollen and spores) and acritarchs were also counted and are presented for the samples where they could be confidently determined and checked by one analyst ($n = 60$). Percentages of single dinocyst groups and species were calculated relative to total dinocyst counts, as well as the total percentage of dinocysts relative to all palynomorphs (i.e., including terrestrial palynomorphs and acritarchs). Furthermore, given the robust, astronomically tuned age model for Site 959, we calculated dinocyst AR normalized by TOC (n cysts cm^{-2} kyr^{-1}). Previous work has shown that ARs correlate with surface water chlorophyll-a concentrations and it is therefore a good indicator for cyst production and nutrient availability (Zonneveld et al., 2009). All materials are stored in the collection of the Laboratory of Palaeobotany and Palynology at the department of Earth Sciences, Utrecht University.

3.3.2. Dinoflagellate Cyst Paleoecology

Dinoflagellates are unicellular, eukaryotic, mostly planktonic protists that occur in all aquatic environments but with highest diversity in the marine realm (Fensome, 1993). Dinoflagellates have several trophic strategies and can be heterotrophic, mixotrophic and autotrophic. The geographical distribution of heterotrophic dinoflagellates, mostly belonging to the Protoperidiniacaea family, is highly dependent on food availability, while that of autotrophic taxa, mostly Gonyaulacoid, is determined by for example, salinity, surface water temperature and nutrient availability (Marret et al., 2020; Zonneveld et al., 2013).

Approximately 15% of marine dinoflagellates produce organic-walled cysts (i.e., dinocysts), which preserve well in marine sediments (Fensome, 1993). Palaeoecological implications of dinocysts occurrences are typically extrapolated from the modern for extant species, which is typically the dominant component of Miocene assemblages (De Schepper et al., 2011; Hannah, 2006; Hoem et al., 2021; Louwye et al., 2007; Quaijtaal et al., 2014; Sangiorgi et al., 2018, 2021; Schreck et al., 2017). For extinct species, inferences are typically based on empirical information (De Schepper et al., 2011; Frieling & Sluijs, 2018; Pross & Brinkhuis, 2005).

Here, we divide the dinocyst taxa in two main groups: Gonyaulacoid and Protoperidiniceae. The latter group of dinocysts derive from obligate heterotrophic dinoflagellates and therefore indicate sufficient food supply (Brinkhuis et al., 1992; Sluijs et al., 2005). Based on previous work on Early to Middle Miocene palynological assemblages at Site 959, these dinocyst taxa could be further assigned to more specific environmental niches (Awad & Oboh-Ikuenobe, 2019; Oboh-Ikuenobe et al., 1999). Certain Gonyaulacoid dinocyst taxa are interpreted to represent offshore environments, that is, *Batiacasphaera* spp. (Schreck & Matthiessen, 2013), *Cerebrocysta* spp. (Pross & Brinkhuis, 2005), *Hystrichokolpoma* spp. (Pross & Brinkhuis, 2005), *Impagidinium* spp. (Jaramillo & Oboh-Ikuenobe, 1999; Pross & Brinkhuis, 2005), *Nematosphaeropsis* spp. (Harland, 1983; Pross & Brinkhuis, 2005; Wall et al., 1977), *Operculodinium* spp. (Harland, 1983; Wall et al., 1977), and *Spiniferites* spp. (Brinkhuis & Zachariasse, 1988; Jaramillo & Oboh-Ikuenobe, 1999; Wall et al., 1977). Furthermore, we regard taxa including *Lingulodinium* spp. (Jaramillo & Oboh-Ikuenobe, 1999; Zevenboom et al., 1994) and *Cleistosphaeridium* spp. (Jaramillo & Oboh-Ikuenobe, 1999; Köthe, 1990) to indicate outer-to-inner-neritic conditions. Finally, *Polysphaeridium* cpx. and *Homotryblium* spp. are typically found in restricted-marine (i.e., lagoon) conditions with lower salinities (Jaramillo & Oboh-Ikuenobe, 1999; Köthe, 1990). Protoperidinioid taxa include *Lejeunecysta* spp. and *Selenopemphix* spp. It was shown that organic cysts produced by heterotrophic Protoperidinioid dinoflagellates are relatively more sensitive to oxic degradation compared to cysts produced by phototrophic Gonyaulacoid dinoflagellates (Zonneveld et al., 1997). Therefore, a considerable presence of well-preserved Protoperidinioid dinocyst taxa has been used as an indicator for the degree of preservation of the analyzed palynology samples.

Modern and relatively recent dinocyst assemblages close to Site 959, taken from recent marine sediments from the (western) Gulf of Guinea, comprise dominantly of *Spiniferites* spp. and *Operculodinium* spp., and lesser abundances of *Impagidinium* spp., *Nematosphaeropsis* spp. and Protoperdiniaceae including *Brigantedinium* spp. and *Echinidinium* spp. (Marret, 1994; Marret et al., 2008).

3.3.3. Statistical Analysis

Detrended Correspondence Analysis (DCA) and Canonical Correspondence Analysis (CCA) on the dinocyst assemblages were performed using the "vegan" R package (Oksanen et al., 2022). CCA analyses was carried out to evaluate the correspondence of dinocyst taxa to environmental indicators, including geochemical proxy records, TEX_{86}-based SST, biogenic Barium (Ba_{bio}) and wt% $CaCO_3$. Higher resolution data sets were linearly interpolated to the sampling resolution of the palynology. Because dinocyst assemblages occasionally comprise of less than 100 specimens and taxa could not consistently be identified on species-level, we did not perform diversity analyses to avoid bias by under-representation.

4. Results

4.1. Total Organic Carbon

On average, the %TOC decreases across the onset of the MCO from average values of 0.6% between 18.2 and 17.7 Ma, to ∼0.4% between 16.9 and 15.0 Ma (Figure 3e). This is also evident from the gradually lighter sediment color, reflected in the greyscale record in Wubben et al. (2023). Prior to the MCO onset, multiple %TOC peaks of
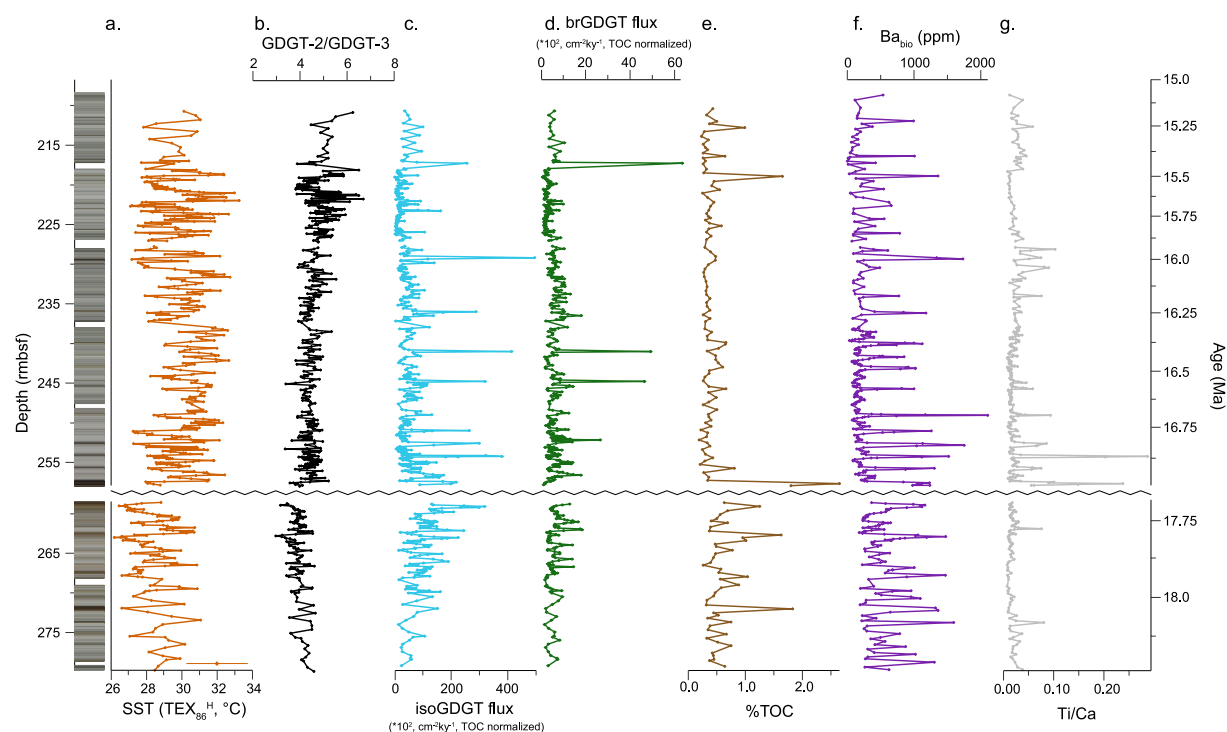
Figure 3. Early to Middle Miocene proxy records from Ocean Drilling Program Site 959 plotted against depth (rmbsf-scale, left) and age (Ma, right). (a) TEX_{86}-SST calibrated with the exponential TEX_{86}^{H} by Kim et al., 2010 (dark orange). (b) GDGT-2/GDGT-3 ratio. (c, d) isoGDGT (light blue) and brGDGT (green) accumulation rates, normalized by TOC. (e) %Total organic carbon. (f) Biogenic barium, proxy for export productivity. (g) Ti/Ca ratio, proxy for dust supply.

~1.0–2.0% are recorded which are spaced approximately 100 kyr apart (at 18.0, 17.9, 17.8, and 17.7 Ma). At the MCO onset (~16.9 Ma), the %TOC record is characterized by a transient peak to 2.7% which occurs simultaneously with peak values of Ba_{bio} and Ti/Ca, and by a persistent increase in MS values (Spiering et al., 2024; Wubben et al., 2023). Two %TOC peaks are recorded at 15.50 and 15.25 Ma with values up to 1% and 1.7%, respectively.

Throughout the Site 959 record, %TOC shows a robust, apparent logarithmic, positive correlation with Ba_{bio} ($r^2 = 0.63$), a proxy for export productivity. Immediately following the MCO onset (16.9–16.5 Ma), Ba_{bio} peaks denote relatively organic-rich, bio-siliceous sedimentary intervals paced by a combination tone of precession and obliquity (Spiering et al., 2024).

4.2. GDGT Concentrations and Relative Abundances

The GDGT pool is dominated by isoGDGTs (~80%), particularly crenarchaeol and GDGT-0 have continuously high abundances. The average, TOC-normalized isoGDGT AR is 6.4×10^3 ($\pm 6.1 \times 10^3$) ng cm^{-2} kyr^{-1}, with peak values up to $\pm 5.0 \times 10^4$ ng cm^{-2} kyr^{-1} (Figure 3c). IsoGDGT AR shows an increasing trend between 18.2 and 17.7 Ma toward values up to 3.0×10^4 ng cm^{-2} kyr^{-1}. Between 17.0 and 16.6 Ma, isoGDGT AR peaks up to 3.5×10^4 ng cm^{-2} kyr^{-1} occur spaced approximately 50 kyr apart, starting at the MCO onset (~16.9 Ma; Figure 3c). Toward the Middle Miocene, isoGDGT AR peaks occur at ~16.6, ~16.4, ~16.3, ~16 and ~15.5 Ma. The average, TOC-normalized brGDGT AR is much lower ($5.3 \times 10^2 \pm 4.8 \times 10^2$ ng cm^{-2} kyr^{-1}), but the record does exhibit striking peaks of $>5.0 \times 10^3$ ng cm^{-2}kyr^{-1} at ~16.5, ~16.4, and up to 6.3×10^3 ng cm^{-2} kyr^{-1} at ~15.4 Ma (Figure 3d). Both isoGDGT and brGDGT ARs are on average higher prior to the MCO onset (~18.3– 17.7 Ma). Furthermore, iso- and brGDGT ARs show similarly paced variability following the onset of the MCO (~16.9–16.6 Ma) to other geochemical records (e.g., MS, Ba_{bio}, Ti/Ca and wt% $CaCO_3$; Spiering et al., 2024; Wubben et al., 2023), that is, relatively high amplitude variability paced by ~55 kyr cycles.

Of the in total 567 TEX_{86} measurements, 3 TEX_{86} values were discarded based on high ΔRI values (0.32–0.37; Zhang et al., 2016) (Figure S1 in Supporting Information S1). Five samples yielded BIT values that exceeded 0.4

which could point at a potential bias of TEX_{86} by soil-derived isoGDGTs (e.g., Weijers et al., 2006) (Figure S1 in Supporting Information S1). However, variability in the BIT index is mainly forced by isoGDGT ARs as the BIT index represents a closed-sum between isoprenoid and branched GDGTs (Hopmans et al., 2004). Moreover, given the likely absence of soil input (i.e., rivers) to Site 959, we do not exclude TEX_{86} values based on the BIT index. Furthermore, 5 TEX_{86} measurements were excluded due to high values of the methanogenesis indicators (GDGT-2/cren, Weijers et al., 2011; and/or Methane Index, Zhang et al., 2011) (Figure S1 in Supporting Information S1). No TEX_{86} measurements exceeded the set cut-off value for the GDGT-0/cren index (Blaga et al., 2009) (Figure S1 in Supporting Information S1), indicating no considerable contribution by GDGTs produced by methanogenic archaea. Throughout the record, GDGT-2/GDGT-3 values remain relatively stable and show an increase from ∼4 (±0.4) prior to the onset of the MCO (∼18.2–17.6 Ma) to ∼5.1 (±0.6) toward the Middle Miocene (∼15.5 Ma), except for 1 low value of 2.3 at ∼15.55 Ma (Figure 3b). Such GDGT-2/GDGT-3 values indicate dominant production of- and/or export of GDGTs from between ∼50–200 m water depth (Hurley et al., 2018; Rattanasriampaipong et al., 2022; Taylor et al., 2013; van der Weijst et al., 2022). Even though GDGT-2/GDGT-3 values exceeding 5 suggest a small component of GDGTs derived from slightly deeper in the water column (Rattanasriampaipong et al., 2022; Taylor et al., 2013), we do not exclude the corresponding TEX_{86} values from our record because their influence on TEX_{86} is rather small (Varma et al., 2023). Rather, we acknowledge a small, but relatively constant contribution to the GDGT pool by deeper dwelling archaea during the Early and Middle Miocene at Site 959. This is in line with results from the Middle to Upper Miocene section at Site 959 that shows elevated (∼5–10) GDGT-2/GDGT-3 values (van der Weijst et al., 2022). Evidently, absolute SST values should be taken with care, but the direction, relative amplitude, and timing of changes in the TEX_{86}-based SST record can be considered robust.

4.2.1. SST

The SST record at Site 959 ($n = 554$) shows a warming of ∼1.5°C, based on the TEX_{86}^{H} calibration, from the earlier Miocene (∼18.3–17.7 Ma; average SST 28.4°C) to the MCO (<16.9 Ma; average SST 29.9°C, Figure 3a). Prior to the MCO, SST variability of ±4°C follows 100 kyr eccentricity cycles (Spiering et al., 2024). Two 100 kyr eccentricity SST peaks between ∼17.9–17.7 Ma show a remarkable asymmetric shape which could point to an influence of high-latitude glacial variability (Spiering et al., 2024). Following the onset of the MCO (∼16.9–16.5 Ma), SST variability remains remarkably high and even increases to on average ±5°C. However, in this interval the SST variability is paced by a combination tone of precession and obliquity, resulting in a ∼55 kyr cycle (Spiering et al., 2024). This interval falls within a node of the long ∼2.4 Myr eccentricity cycle, causing a relative increase in the expression of obliquity (Spiering et al., 2024), which is also evident from the absence of clear ∼400 kyr eccentricity amplitude modulation relative to the interval between ∼16.5–15.0 Ma (Figure 3a). Lowest SSTs correlate to pronounced Ba_{bio} peaks and increased Ti/Ca values.

Between 16.5–15.0 Ma, SST reaches peak values during 400 kyr eccentricity maxima at ∼16.4, ∼16.0, and ∼15.6 Ma up to ∼32.5, ∼32.8, and ∼33.2°C respectively (Figure 3). Throughout this interval, SST shows prominent high amplitude variability paced by short (∼100 kyr) eccentricity and, in intervals where the sampling resolution is sufficient, by precession (i.e., 15.8–15.5 Ma). Between 16.5–15.0 Ma, a negative correlation between %TOC and SST is observed, except for the period between ∼16.3–15.8 Ma which shows significantly less %TOC variability.

Highest SSTs at 15.6 Ma correspond to MCO peak warming, which was previously identified in the bulk carbonate $\delta^{18}O$ record at Site 959 (Wubben et al., 2023), and in published benthic foraminiferal $\delta^{18}O$ records from the eastern equatorial Pacific (Holbourn et al., 2015).

4.3. Palynology

Dinocyst preservation varies from good to poor and ARs are low, averaging 2×10^3 cysts cm^{-2} kyr^{-1} (Figure 4). Transient peaks occur between ∼17.0–16.7 Ma (±4×10^3–12×10^3 cysts cm^{-2} kyr^{-1}) and at 15.7 Ma (±6×10^3 cysts cm^{-2} kyr^{-1}). Especially between ∼17–16.7 Ma, variability is high with ARs varying between ±1×10^3–12×10^3 cysts cm^{-2} kyr^{-1}, paced by obliquity and precession (Figure 4). Besides dinoflagellate cysts, palynological residues are often dominated by pyritized bio-siliceous material such as diatom and radiolarian fragments and contain varying abundances of amorphous organic matter, that is, structureless and unidentifiable organic particles, organic test linings of benthic foraminifera, organic linings of calcareous dinocysts and occasionally
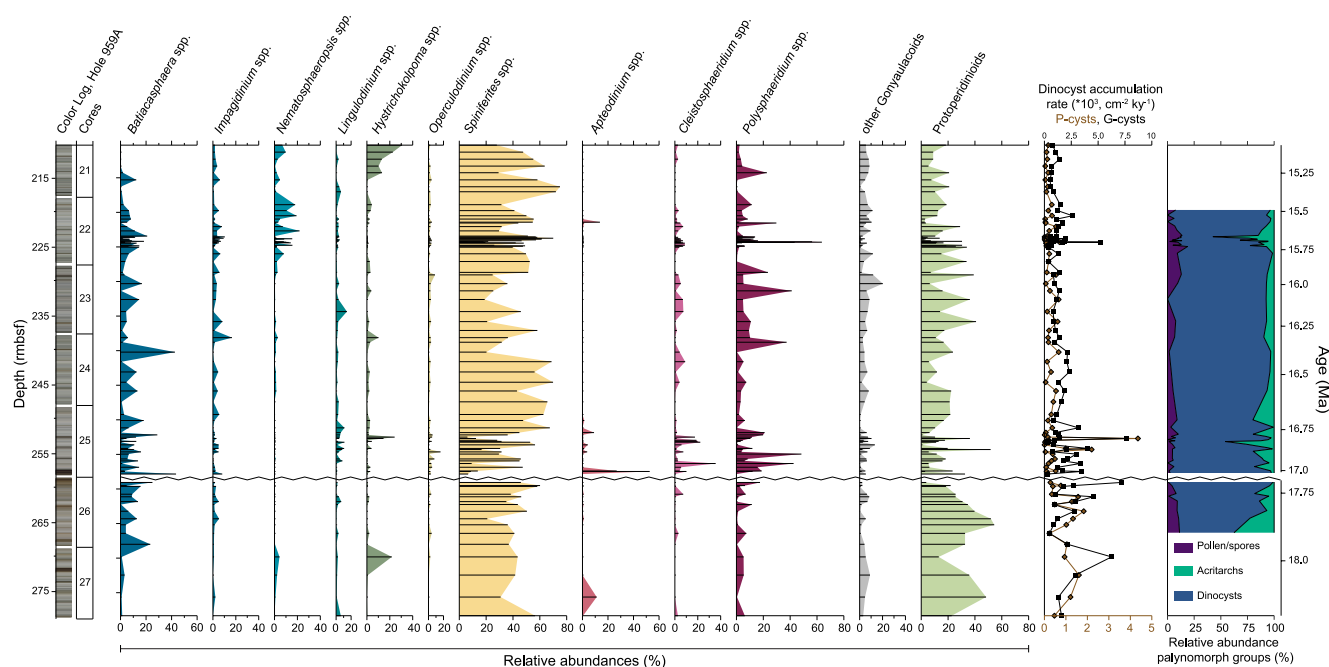
Figure 4. Most important groups of Early to Middle Miocene dinocyst assemblages at Site 959 plotted against depth (rmbsf scale, left) and age (Ma, right). Dinocyst accumulation rates in brown and black graphs (cysts × 10^3 cm^{-2} ky^{-1}). Areaplot shows relative abundances of the three palynomorph groups; dinocysts, acritarchs and, pollen and spores.

degraded phytoclasts. Pollen and spores, mostly represented by trilete spores and triporate pollen, are present throughout the record but only make up on average 5%–10% of the total palynomorph assemblage (Figure 4). ARs of terrestrial palynomorphs are on average 0.15×10^3 palynomorphs cm^{-2} kyr^{-1}, with highest values up to 0.4×10^3–1.0×10^3 cysts cm^{-2} kyr^{-1} prior to the MCO and immediately following the MCO onset (~16.9–16.7 Ma). Finally, the prasinophyte algae *Cymatiosphaera* spp. is encountered sporadically but always comprise <5% of the total palynomorph assemblage. Acritarch abundances average ~10% of the total palynomorph assemblage (2.5×10^2 acritarchs cm^{-2} kyr^{-1}) but are high between 16.9–16.6 Ma (peaks ~20–45%; ~4×10^2 cysts cm^{-2} kyr^{-1}) and between 15.7–15.6 Ma (~20–55%; >1.0×10^3 cysts cm^{-2} kyr^{-1}). This group comprises small (~10 μm), round skolochorate cysts with numerous spines of variable lengths and occasional septa.

Despite the variable preservation, we do not expect a significant oxidation bias given that well-preserved Protoperidinioid cysts were found throughout the record. Dinocyst assemblages are generally dominated by Gonyaulacoid cysts with highest abundances of the cosmopolitan *Spiniferites* spp. (5%–75%) and common taxa like *Batiacasphaera* spp. (7%–45%), *Cleistosphaeridium* cpx. (also including *Adnatosphaeridium* spp.; 4%–25%), *Hystrichokolpoma* spp. (mostly *H. rigaudiae*; 3%–30%), *Impagidinium* spp. (3%–15%), *Lingulodinium* cpx. (mostly *L. machaerophorum*; 2%–13%) and *Operculodinium* spp. (2%–15%) (Figure 4, Figure S2 in Supporting Information S1). Goniodomidae group *Polysphaeridium* cpx. (mostly *P. zoharyi* and including *Homotryblium* spp.) is present throughout the record (6%–32%), occasionally showing peak abundances. *Apteodinium* spp. is encountered at several intervals in the record and exhibits peak abundances immediately following the onset of the MCO (~16.95 Ma; 25%–45%) and at ~15.6 Ma (~13%). Furthermore, *Nematosphaeropsis labyrinthus* is present in relatively low quantities between 18.2–15.8 Ma (~0%–5%) but becomes more abundant between 15.8–15.0 Ma (up to ~22%). *Heteraulacacysta* spp. (mostly *H. campanula*) and *Tuberculodinum vancampoae* occur sporadically at relatively low abundances (~0%–5%) (Figure 4). Protoperidinioid dinocysts are common throughout the record (~18%) and dominantly include *Brigantedinium* spp. (mostly *B. simplex*), *Lejeunecysta* spp. (mostly *L. attenuata*, *L. cinctoria* and *L. fallax*), and *Selenopemphix* spp. (mostly *S. nephroides* and *S. selenoides/undulata*). A complete overview of dinocyst taxa is presented in Figures S3–S5 in Supporting Information S1.

4.3.1. Dinoflagellate Cyst Paleoenvironmental Interpretations

Continuous dominance of Spiniferites spp. and presence of Batiacasphaera spp. and Impagidinium spp. support previous inferences of a relatively warm, open ocean setting at Site 959 throughout the Early to Middle Miocene, with periodic influx of (inner-)neritic taxa. The consistent presence of Protoperidinioid dinocysts, produced by obligate heterotrophic dinoflagellates, indicates sufficient food supply, consistent with the diatom-rich sediments. Moreover, increased Protoperidinioid dinocysts are typically found in dark, diatom-rich sediments, consistent with increased productivity at the time of deposition.

Prior to the onset of the MCO (~18.2–17.7 Ma), the relative abundance of Protoperidinioid cysts is high (~30%) and their abundances seem to be paced by eccentricity, with peak abundances up to ~55% during eccentricity minima. Relatively increased cyst production by heterotrophic dinoflagellates in this interval (18.5–17.7 Ma) is supported by relatively high total dinocyst and P-cyst ARs (~9.3×10^2 cysts cm^{-2} kyr^{-1} and ~3.5×10^3 cysts cm^{-2} kyr^{-1}, respectively) compared to the MCO (<17.0 Ma; ~3.0×10^2 cm^{-2} kyr^{-1} and ~1.7×10^3 cm^{-2} kyr^{-1}, respectively). Furthermore, *Batiacasphaera* spp. and *Spiniferites* spp. are abundant and a peak abundance of *Hystrichokolpoma* spp. (~20%) occurs at 17.95 Ma. Collectively, this points to open ocean waters with eccentricity-paced episodes of enhanced nutrient availability to support high Protoperidiniacaea abundances.

The MCO onset is characterized by peak abundance of *Apteodinium* spp. (~45%) at ~16.95 Ma, followed by highly variable abundances of taxa that are typically known from (inner-)neritic and lagoonal settings and favor relatively warm conditions; *Cleistosphaeridium* cpx. (~25%), *Polysphaeridium* cpx. (~45%) and *T. vancampoae* (~3%). These taxa alternate with increased relative Protoperidinioids and other Gonyaulacoid taxa (i.e., *Batiacasphaera* spp., *Lingulodinium* spp. and *Operculodinium* spp.) paced by the combination tone of precession and obliquity (~55 kyr). Furthermore, total dinocyst ARs are comparably higher in this interval (~17.0–16.6 Ma). During the early phase of the MCO, oceanographic conditions seem considerably variable, with dinocyst assemblages implying warmer, stratified waters that alternate with increased nutrient availability paced by precession and obliquity.

From 16.6 Ma to the youngest part of the record, the amplitude variability in dinocyst abundances decreases and the assemblage becomes more uniformly dominated by *Spiniferites* spp. (~20–70%), with *Polysphaeridium* cpx. (~5–20%) and Protoperidiniaceae (~5–35%) between ~16.6–15.8 Ma. We should note that a relatively lower temporal resolution of the palynological record in this interval could have affected the apparent decrease in dinocyst abundance amplitude variability. However, this change in general dinocyst abundances coincides with a shift to CaCO$_3$-dominated lithologies at the cost of bio-siliceous material, suggesting it could reflect a true signal. At ~15.7 Ma, the record is characterized by a transient peak in *Polysphaeridium* cpx. abundance (~30%, 3.78×10^3 cysts cm^{-2} kyr^{-1}), which correlates with increased absolute concentrations of *Nematosphaeropsis* spp. (~6×10^3 cysts cm^{-2} kyr^{-1}) and Protoperidinioid cysts (~7×10^3 cysts cm^{-2} kyr^{-1}). In the youngest part of the studied interval, N. labyrinthus becomes one of the dominant taxa (~10–20%) together with *Spiniferites* spp., which is comparable to modern dinocyst assemblages in the region, that is, more open ocean conditions close to oceanic fronts. *N. labyrinthus* is specifically abundantly found in the upwelling region of the modern eastern equatorial Atlantic (Marret, 1994). Furthermore, highest resolution dinocyst analyses between ~15.8–15.5 Ma reveals conspicuous alternating abundances of *Nematosphaeropsis* spp. and *Polysphaeridium* cpx. on precession timescales, whereby the latter has a striking peak abundance at ~15.7 Ma (~30%, ~3.8×10^3 cysts cm^{-2} kyr^{-1}).

4.3.2. Statistical Analyses

DCA and CCA analyses of the dinocyst assemblage, including dinocyst groups that represent at least 5% of the total dinocyst assemblage or are otherwise grouped in a "G-cyst rest" group, show that the variability is governed by *Apteodinium* spp. and *Hystrichokolpoma* spp. (Figure 5a), which plot together toward Ba$_{bio}$ on CCA axis 2 (Figure 5b). DCA axis 1 (eigenvalue: ~0.22) shows a division of *Polysphaeridium* cpx. and *Cleistosphaeridium* cpx. on one side, and *Nematosphaeropsis* spp., *Spiniferites* spp. and *Batiacasphaera* spp. on the other side. Based on palaeoecological interpretations, this division represents a signal between warm and conditions typical for more (inner-)neritic and/or lagoonal settings (i.e., by the occurrence of *Polysphaeridium* cpx., *Cleistosphaeridium* cpx. and *Apteodinium* spp.) versus more open ocean conditions represented by *Nematosphaeropsis* spp., *Spiniferites* spp. and *Batiacasphaera* spp. (Schreck & Matthiessen, 2013; Wall et al., 1977; Zonneveld et al., 2013). Considering the offshore setting of Site 959 during the Miocene, it could be hypothesized that the latter groups represent in-situ taxa while the (inner-)neritic to lagoonal taxa could have been transported from the
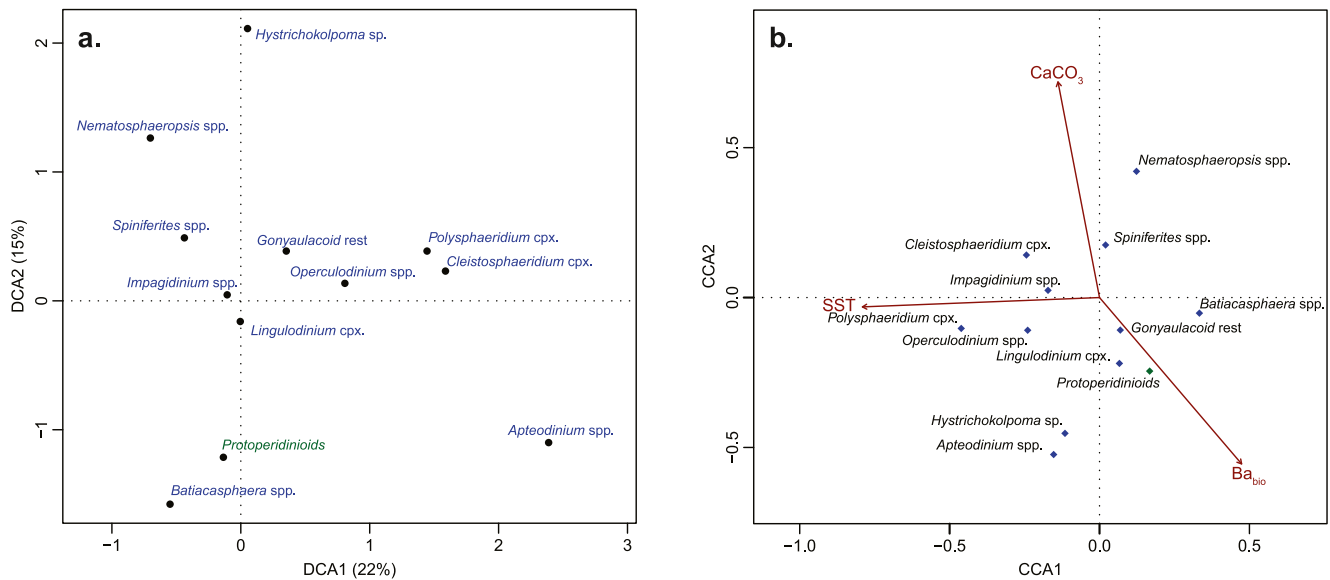
Figure 5. Results of statistical analyses on dinocyst assemblages of Site 959. (a) Detrended Correspondence Analysis (DCA) output with Gonyaulacoid- and Goniodomid taxa in blue and Protoperidioid group in green. (b) Canonical Correspondence Analysis (CCA) output.

shelf. However, comparison to other geochemical proxy records is necessary to verify this. Furthermore, the Protoperidinioid group and *Batiacasphaera* spp. closely correspond along DCA axis 2, while they respond oppositely to *Hystrichokolpoma* spp. and *Nematosphaeropsis* spp. CCA results show that the Protoperidinioid group corresponds closely to Ba_{bio}, following previous interpretations of increased Protoperidinioid cysts production by heterotrophic dinocysts during increased nutrient conditions. More specifically, it seems that increased Protoperidinioid dinocysts coincide with phases of increased biogenic opal production (i.e., high Ba_{bio}) by diatoms, indicated by the dark, bio-siliceous-rich layers deposited between ~18.5–16.5 Ma (Figure 2; Wubben et al., 2023). Conversely, *Nematosphaeropsis* spp. plots closely to $CaCO_3$ on CCA axis 2 which supports "open ocean" conditions and potentially represents increased carbonate production relative to opal toward the Middle Miocene portion of the Site 959 record. As previously shown in Wubben et al. (2023), a shift in the depositional system occurs at ~16 Ma whereby increased productivity becomes characterized by elevated $CaCO_3$ deposition instead of biogenic silica. Therefore, increased relative abundances of *Nematosphaeropsis* spp. between ~16–15 Ma seems to further demonstrate this shift in depositional dynamics at Site 959.

5. Discussion

5.1. SST Across the MCO

Average absolute SSTs during the MCO (~17–15 Ma) varied from ~27 to 33°C (Figure 3). With the TEX_{86}^H calibration, this is ~2–5°C warmer than the present-day seasonal SST range in the eastern equatorial Atlantic (~25.0–28.5°C; Locarnini et al., 2013). During the later stages of the MCO (15–13 Ma), average SSTs were ~30°C at Site 959 (Van der Weijst et al., 2022), consistent with the MCO portion of the SST record presented in this study. An abrupt increase of GDGT-2/GDGT-3 values from approximately 5 to 7 points to a downward expansion of the GDGT export zone at the MMCT (~13.6 Ma), hypothesized to be associated with a Middle to Late Miocene cooling trend in the TEX_{86} (van der Weijst et al., 2022). We also record a gradual increasing trend in GDGT-2/GDGT-3 values during the Early to Middle Miocene from ~16.3–15.0 Ma (Figure 3), albeit less steep than at ~13.6 Ma, and therefore a shallow subsurface calibration might be more relevant here. However, since the relationship between temperature change in the surface and subsurface is 1:1 over longer timescales (Ho & Laepple, 2016), a subsurface calibration could accurately represent SST changes as well (Figure S2 in Supporting Information S1). Moreover, we find a poor correlation between TEX_{86} and GDGT-2/GDGT-3 ($r^2 = 0.18$), suggesting that GDGTs potentially produced in the sub-surface do not have a significant effect on our reconstructed SSTs.
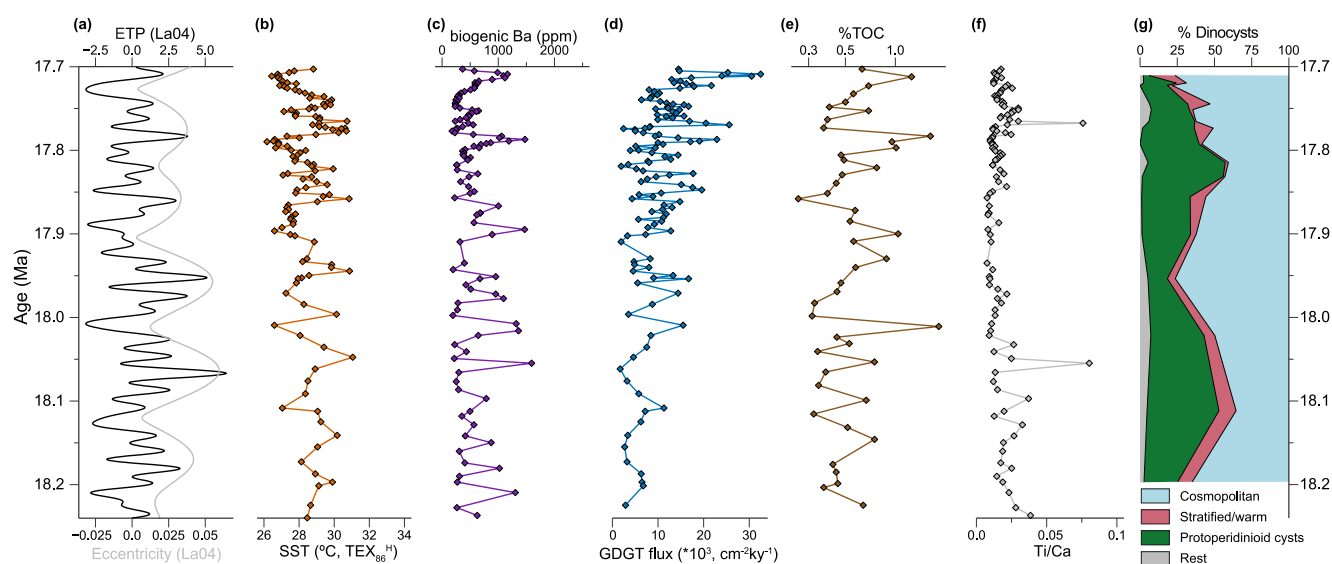
Figure 6. Compilation of geochemical- and palynology proxy records immediately prior to the Miocene Climatic Optimum onset (~18.25–17.7 Ma) at Site 959. (a) Eccentricity, Tilt, Precession (ETP; black) and Eccentricity (gray) from Laskar et al. (2004). (b) TEX_{86}-SST calibrated with exponential calibration TEX_{86}^{H} of Kim et al. (2010). (c) Biogenic barium. (d) TOC-normalized accumulation rate of total GDGTs. (e) %Total Organic Carbon (TOC) plotted on a logarithmic scale. (f) Ti/Ca ratio, indicator for dust supply. (g) Area plot showing relative abundances (%) of major dinocyst groups.

SSTs at the onset of the MCO were ~1.5°C higher than background values of 28.7 ± 2.3°C between ~17.7–18.5 Ma. Even though the Site 959 sedimentary record does not completely capture the MCO onset due to a hiatus and/or a condensed lithological interval (Wubben et al., 2023), this is the first low-latitude SST record covering the MCO onset and associated warming (see Sosdian et al., 2024 for a Miocene SST compilation). Increasing abundances of the thermophilic *Polysphaeridium* cpx. between 16.95–16.60 Ma aligns with the warmer SSTs detected at the MCO onset at Site 959. In comparison, North Atlantic TEX_{86} and $U^{k'}_{37}$-based SST reconstructions imply relatively warm conditions during the MCO, although they do not reflect a significant warming at the MCO onset but rather gradual warming since the Early Miocene (Herbert et al., 2020; Super et al., 2018, 2020). A lack of clear MCO warming in the North Atlantic basin might be ascribed to regional changes related to dynamic circulation patterns, that is, polar gyres and Meridional Overturning Circulation (MOC) initialization, and establishment of ocean gateways during the Early and Middle Miocene. Rather, both short- and long-scale SST variability at Site 959 is similar to benthic $\delta^{18}O$ records from the equatorial Pacific, including warming at the MCO onset (Holbourn et al., 2015). Furthermore, SST changes throughout the Site 959 record show strong Milankovitch cyclicity, most notably ~100 kyr, ~400 kyr and ~2.4 Myr eccentricity, which is in line with Early and Middle Miocene isotope stratigraphy and supports the global nature of MCO warming recorded at Site 959 (Beddow et al., 2016; Holbourn et al., 2007, 2015; Liebrand et al., 2016).

5.1.1. Cooling Toward the Middle Miocene

Even though SST variability remains high throughout the entire MCO interval, average SST decreases by ~1°C between ~16.05–15.85 Ma, coinciding with a ~400 kyr eccentricity maximum at 16 Ma (Figures 3 and 9). A similar "cooling" trend is recorded in the equatorial Pacific $\delta^{18}O_{benthic}$ record, indicating a global trend (Holbourn et al., 2015; Kochhann et al., 2017) (Figure 2). Coeval cooling was also recorded at a continental shelf-site drilled in the Porcupine Basin (Sangiorgi et al., 2021). Collectively, it seems this cooling was global in nature. In the Porcupine Basin, this cooling corresponds to increased productivity indicated by dinoflagellate cyst proxies, supporting potential enhanced carbon burial contributing to CO_2 drawdown and subsequent cooling. Dinoflagellate cyst assemblages at Site 959 do not imply an increase in productivity (i.e., increased Protoperidinioid cysts) in this interval. However, the cooling trend does coincide with a decrease in wt% $CaCO_3$ and a relative increase in terrigenous material, that is, clays (MS) and dust (Ti), and peak Ba_{bio} and %TOC values (Figures 2 and 3), indicating increased surface water productivity and terrigenous material input to Site 959.

Moreover, the cooling trend coincides with the (first) zenith of the carbon isotope Monterey Excursion (CM-3), recorded in global $\delta^{13}C_{benthic}$ records (Holbourn et al., 2004, 2007, 2015; Lear et al., 2010; Sosdian et al., 2020), as well as in the bulk carbonate $\delta^{13}C$ record of Site 959 (Wubben et al., 2023) (Figure 2). Consequently, the drop in both deep-marine and surface ocean temperatures at this time could have been caused by increased organic carbon burial along continental margins during a time of elevated CO_2 concentrations, which acted as a negative carbon cycle feedback (i.e., the Monterey Excursion, Sosdian et al., 2020; Vincent & Berger, 1985). To facilitate this increased burial and the resulting cooling, the long-term negative carbon cycle feedback associated with the ME would have needed to prevail over the positive carbon cycle feedback mechanism linked with the shorter-scale CM-events as previously described by Sosdian et al. (2020). During the ~400 kyr eccentricity maxima at 16.8 Ma (CM-1) and 16.4 Ma (CM-2), we record comparably less (shorter-scale) variability than during the eccentricity maxima at 16 Ma (CM-3) and 15.6 Ma (CM-4). This might be ascribed to decreased ~100 kyr eccentricity power compared to the subsequent ~400 kyr eccentricity maxima at 16 Ma and 15.6 Ma due to a node in the 2.4 Myr eccentricity cycle. Therefore, the cooling trend at 16 Ma at Site 959 could have been amplified relative to other ocean basins by intensified upwelling of colder waters during ~400 kyr eccentricity minima. Moreover, this suggests that after ~16.4 Ma, upwelling intensity at Site 959 was amplified on ~400 kyr eccentricity timescales, akin to the phasing recorded in the pre-MCO interval at this site.

At Site 959, we do not record significantly increased SSTs during the eccentricity maximum at ~15.6 Ma, previously called "peak warming" of the MCO (Holbourn et al., 2015). This finding is supported by relatively subdued amplitude of variability in the bulk carbonate $\delta^{18}O$ at ~15.6 Ma at Site 959 (Wubben et al., 2023). Notably, SST was similarly elevated during other eccentricity maxima during the MCO. Other biomarker-based SSTs do not record significant warming at 15.6 Ma either, but is should be noted that the temporal resolution of these records is comparably lower (Herbert et al., 2020; Sangiorgi et al., 2021; Super et al., 2018, 2020). This absence of a striking warming at 15.6 Ma is in contrast to benthic foraminiferal $\delta^{18}O$ and bottom water temperatures (BWT) from the eastern equatorial Pacific, where a distinct ~2.6°C warming is recorded (Site U1337; Holbourn et al., 2007, 2015; Kochhann et al., 2017). As eastern equatorial Atlantic BWTs are derived from colder waters sourced from higher latitudes, a lack of SST "peak warming" at 15.6 Ma at the tropical location of Site 959 might be explained by higher temperature variability at high latitudes compared to the tropics (i.e., polar amplification).

5.2. Monsoon Forcing of Surface Ocean Dynamics at Site 959

Wubben et al. (2023) and Spiering et al. (2024) showed a strong imprint of eccentricity, obliquity and precession throughout the Early and Middle Miocene proxy records at Site 959 and attributed this to orbitally forced intensity variations of the WAM. Here, we aim to provide a mechanistic explanation of how monsoon intensity variability impacted regional climate and oceanography.

5.2.1. Pre-MCO (~18.3–17.7 Ma)

Prior to the onset of the MCO (>17 Ma), variability in the proxy records is dominantly paced by ~400 and ~100 kyr eccentricity. Notably, SST changes during ~100 kyr eccentricity cycles exhibit a conspicuous asymmetric shape between 17.7 and 17.9 Ma (Figure 6b). Spiering et al. (2024) attribute this asymmetric shape to an influence of high-latitude glacial variability related to prolonged ice-sheet growth and abrupt melting phases, as previously recorded in the Early Miocene (Liebrand et al., 2017). An influence of Southern Ocean climate variability recorded in the TEX_{86} could derive from South Atlantic Central Waters that make up the shallow subsurface at Site 959 (SACW; van der Weijst et al., 2022), which derive from the subtropical front in the Southern Ocean (e.g., Stramma & England, 1999). Via the EUC, SACW are transported to the Gulf of Guinea where they presently occupy sub-thermocline water depths and contribute to seasonal upwelling (Locarnini et al., 2013; Verstraete, 1992). However, even though pre-MCO SSTs seem clearly influenced by high-latitude dynamics on eccentricity timescales, we do not find a similar asymmetric shape in the $\delta^{18}O_{bulk}$ record of Site 959. Moreover, aside from variability over longer timescales (i.e., onset of the MCO), both $\delta^{18}O_{bulk}$ and SST do not exhibit a robust correlation with $\delta^{18}O_{benthic}$ from the eastern equatorial Pacific (Holbourn et al., 2015; Westerhold et al., 2020) during this interval. Therefore, we surmise that variability in $\delta^{18}O_{bulk}$ and SST is most dominantly a function of upper ocean dynamics induced by monsoon circulations on shorter (precession) timescales, while high-latitude ice volume variability likely forces SSTs on longer (eccentricity) cycles.

Lowest SSTs consistently correlate with increased export productivity (i.e., high Ba$_{bio}$), organic carbon (%TOC) preservation and increased abundances of Protoperidinioid cysts during eccentricity minima (Figure 6). This indicates elevated food supply prior to the MCO onset. Higher nutrient availability could have come from enhanced input of (a) fluvially sourced terrigenous material, (b) dust from the arid West African continent and/or from (c) upwelling of nutrient-rich waters. In contrast to the MCO (~17–15 Ma), between ~18.2–17.7 Ma there is a robust positive correlation between MS and dark colored, biogenic silica-rich lithologies (i.e., productivity indicators, Wubben et al., 2023). Furthermore, we find relatively increased abundances of terrestrial palynomorphs between ~17.9 and 17.7 Ma (~0.4 × 10^3 palynomorphs cm^{-2} kyr^{-1}). These findings suggest that terrestrially sourced nutrients may have contributed to fueling increased surface productivity prior to the MCO. However, high MS could reflect increased Fe sourced by dust, rather than merely clays from rivers. Moreover, Site 959 is located approximately 120 km offshore at present day and because of higher sea levels (~40–50 m higher relative to present day; Rohling et al., 2022), the coastline was likely positioned even further inland during the Miocene. Furthermore, the position of Site 959 relative to the shelf-slope break was not significantly different from today during the Early and Middle Miocene (Basile et al., 1998). This means that the influx of fluvially sourced nutrients would have required intense West African offshore surface currents or a major river system to have reached Site 959. Given that the amount of terrestrial material at Site 959 is generally relatively low, and the Niger River delta was far away, also during the Miocene (Grimaud et al., 2018), we surmise that fluvially sourced nutrients did not play an important part in increasing surface water productivity at Site 959.

It was previously proposed that turbidity currents could have caused deposition of terrestrial palynomorphs as well as a lagoonal dinocyst taxa to Site 959 (e.g., Polysphaeridium cpx., Awad & Oboh-Ikuenobe, 2019). However, there is no evidence for disturbed sedimentation or increased clast sizes because of mass flows in the Early and Middle Miocene aged sediment cores (Mascle et al., 1996). Rather, sedimentation is strongly controlled by orbital forcing (Spiering et al., 2024; Wubben et al., 2023). Therefore, it may be possible that seasonal offshore winds transported surface waters offshore, particularly during boreal winter, explaining the occurrences of typical lagoonal dinocyst taxa, and some pollen and spores. Increased seasonal offshore winds could be caused by relatively increased southward displacement of the ITCZ over the southern-West African coast during precession and eccentricity maxima. Offshore winds can be traced by Ti and Fe deposition, which typically resides in aeolian dust and is transported via northeastern (NE) trade winds (i.e., Harmattan winds). Al-normalized Ti and Fe records show similar variability throughout the Early Middle Miocene record at Site 959, with Ti concentrations being consistently somewhat lower than Fe. Previous work has shown that the Ti/Ca ratio is a good indicator for offshore dust flux in tropical West Africa (Tiedemann et al., 1994) and at Site 959 during the Late Miocene to Early Pleistocene (Vallé et al., 2017). Therefore, we apply this ratio as a proxy for dust supply as well. Prior to the MCO, increased Ti/Ca values correspond to Ba$_{bio}$ peaks, suggesting that increased productivity was related to dust supply (Figure 6). Modeling studies show that the onset of considerable aridification of the North African continent occurred during the Early Miocene (Z. Zhang et al., 2014), likely caused by a combination of tectonic changes and greenhouse warming. The high Ti/Ca peaks, as well as its correlation with high Ba$_{bio}$ values at Site 959 potentially support increased aridification of the African continent. This increased aridification likely caused fertilization of the surface ocean by dust, resulting in Ba$_{bio}$ peaks. Furthermore, highest Ti/Ca occur especially during ~400 kyr eccentricity maxima and to a lesser extent during ~100 kyr eccentricity maxima, suggesting that NE trade winds were intensified when the ITCZ was maximally (i.e., by eccentricity modulation of precession) positioned towards the south. Sapropel formation in the Mediterranean during Late Miocene to Pleistocene times show that monsoon-induced atmospheric circulation varied largely on shorter, precession timescales, whereby increased precipitation over North Africa resulted in enhanced Nile River runoff during precession minima (Larrasoaña et al., 2003; Rossignol-Strick, 1985). Given the prominent longer (~100 kyr) eccentricity cyclicity in almost all pre-MCO records at Site 959 (Spiering et al., 2024), WAM circulation was likely less sensitive to changes in insolation compared to Late Miocene to Pleistocene times.

5.2.2. MCO Onset (~17.0–16.6 Ma)

Immediately following the MCO onset and associated relatively warm SSTs, all proxy records show anomalously high amplitude variability on ~20–55 kyr timescales, which is unmatched during the younger part of the MCO (<16.5 Ma; Figure 7). Strikingly high Ba$_{bio}$ peaks (>1,000 ppm) correspond to increased absolute abundances of dinocysts and relatively low SSTs. This suggests that increased export productivity is related to intensified upwelling of colder subsurface waters. At present, coastal upwelling occurs during boreal summer when the EUC
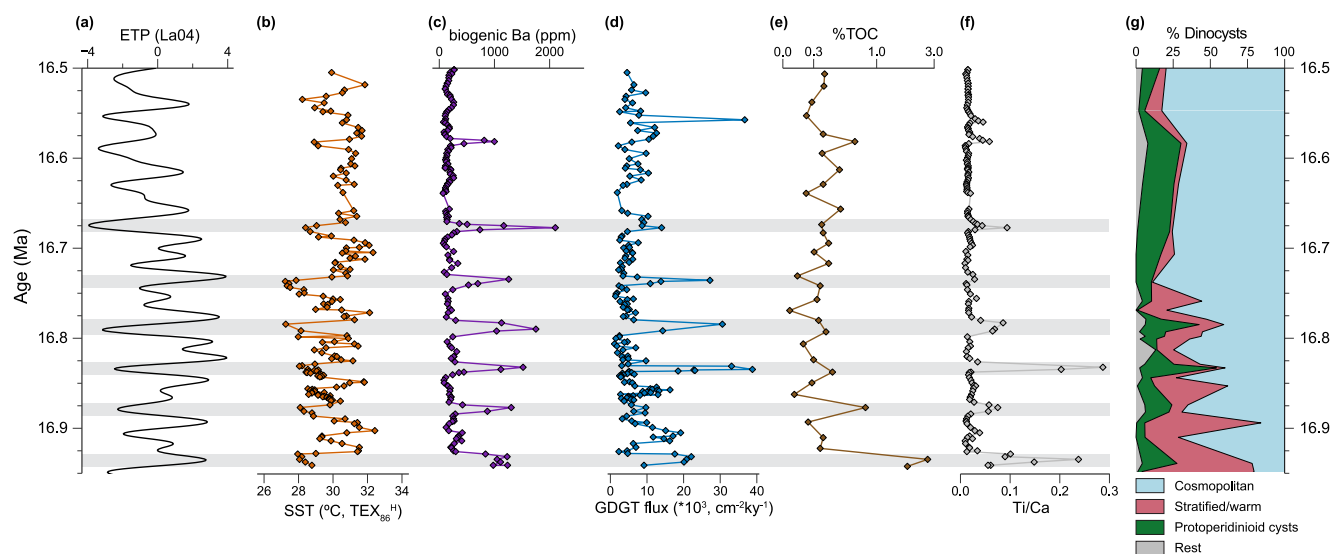
Figure 7. Compilation of geochemical- and palynology proxy records immediately following the Miocene Climatic Optimum onset (~16.95–16.5 Ma) at Site 959. (a) Eccentricity, Tilt, Precession (ETP) from Laskar et al. (2004). (b) TEX$_{86}$-SST calibrated with exponential calibration TEX$_{86}^{H}$ of Kim et al. (2010). (c) Biogenic barium. (d) TOC-normalized accumulation rate of total GDGTs. (e) %Total Organic Carbon (TOC) plotted on a logarithmic scale. (f) Ti/Ca ratio, indicator for dust supply. (g) Area plot showing relative abundances (%) of major dinocyst groups. Horizontal gray bars represent intervals associated with intensified monsoon circulation, decreased sea surface temperatures, coastal upwelling and dust supply.

and NECC converge in the Gulf of Guinea and the ITCZ is located over North Africa. However, because of the more southernly position of the Gulf of Guinea coastline during the Miocene, upwelling likely occurred during boreal winter and was facilitated by westward flowing SEC waters (Norris, 1998; Wagner, 2002). In this case, alongshore westward flow causes offshore Ekman transport of surface waters, thereby creating divergence to facilitate upwelling (Verstraete, 1992). Therefore, when the ITCZ was displaced most southernly during precession maxima, upwelling would have intensified, which caused elevated export productivity from surface waters at Site 959 (Spiering et al., 2024). As was proposed for the Late Miocene to Pleistocene (van der Weijst et al., 2022), and as we surmise for the pre-MCO interval of our records, upwelled waters were likely sourced from SACW, which is approximately 10–20°C colder than the surface waters in the GG. Hence, variations in upwelling strength likely explains the high SST amplitude variability we record between ~17.0–16.6 Ma, and to a lesser extent during our entire Early to Middle Miocene record. Furthermore, within the early MCO interval, increased export productivity indicated by Ba$_{bio}$ peaks correlates with enhanced dust influx, indicated by Ti/Ca peaks (Figure 7). This relationship fits with the modern WAM circulation patterns, whereby NE trade winds (i.e., Harmattan) are increased during boreal winter when the ITCZ is displaced southward. As this increased variability in our SST, export productivity and dust records are unmatched in the younger parts of the MCO (~16.5–15.0 Ma) as well as prior to the MCO onset (~18.2–17.7 Ma), we conclude that WAM circulation was intensified immediately following the onset of the MCO. The strong orbital control on the WAM intensity variations (Spiering et al., 2024) corroborates this conclusion.

During intervals characterized by high SSTs between ~16.9–16.6 Ma, we record peak relative abundances of *Polysphaeridium* cpx., *Cleistosphaeridium* spp. and *Apteodinium* spp., as well as minor abundances of *Tuberculodinium* spp., paced by the ~55 kyr-long precession-obliquity combination tone. These dinocyst taxa are characteristic for (inner-)neritic to lagoonal conditions in modern and past systems. However, the paleodepth at Site 959 during the early MCO was likely similar to present-day at ~2,000 m (Basile et al., 1998; Miller et al., 2020). Hence, these taxa could have been transported to the offshore (a) or could have been produced in-situ (b) in the surface waters of Site 959.

Multiple lines of evidence contradict that offshore transport caused increased periodic abundances of lagoonal and inner-neritic dinocyst taxa following the MCO onset. First, there is no sign of strong episodic sediment transport (e.g., turbidity currents) considering the regular, orbitally driven sedimentological patterns that characterize sedimentation at Site 959 (Mascle et al., 1996; Wubben et al., 2023). Second, terrestrial palynomorphs make up a negligible part of the total palynomorph assemblages and fluxes of soil microbial-derived brGDGTs
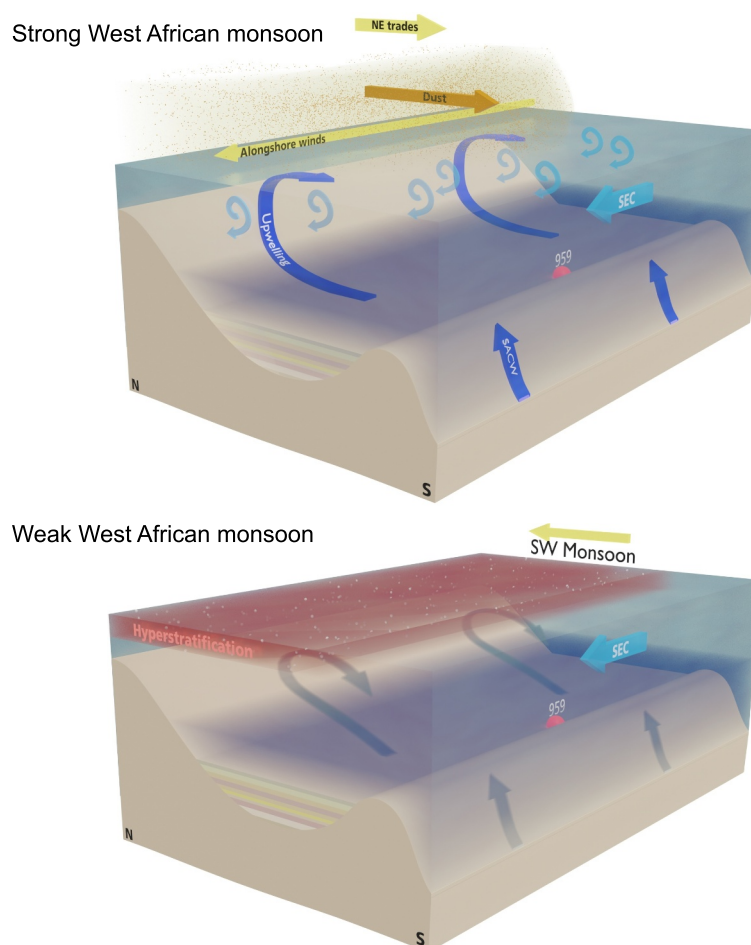
Figure 8. Schematic transect of the continental margin offshore West Africa showing major oceanographical conditions. The position of Ocean Drilling Program Site 959 is shown by the red dot on the Côte d'Ivoire-Ghana Marginal Ridge. Upper panel: major ocean currents at Site 959, influenced by a strong West African Monsoon (WAM) (i.e., strong Northeast (NE) trades). Lower panel: major ocean currents at Site 959, influenced by a weaker WAM (i.e., weak Southwest (SW) Monsoon winds). The red surface ocean indicates enhanced salinities and hyperstratification. SEC = South Equatorial Current, SACW = South Atlantic Central Waters.

are relatively low. We find that increased relative abundances of (inner-)neritic and lagoonal taxa between ~16.95–16.5 Ma correlate to decreased dust supply and upwelling, and relatively high SSTs. These conditions occur during precession (and eccentricity) minima, when WAM circulation is weaker over the Gulf of Guinea and southwest (SW) monsoons and onshore winds prevail. Therefore, typical mechanisms for offshore transport via wind, offshore surface currents and upwelling, were actually reduced in intervals where we find increased abundances of (inner-)neritic and lagoonal dinocyst taxa. Third, there is no correlation between these (inner-)neritic and lagoonal taxa and MS, an indicator for supply of terrestrial material. These lines of evidence imply that offshore transport was not responsible for inner-neritic and lagoonal taxa at Site 959.

Taxa such as *Polysphaeridium* cpx. could have been produced in-situ at Site 959 by extreme stratification of the surface waters, that is, "hyperstratification," analogous to occurrences in the Arabian Sea following glacial overturning events (Reichart et al., 2004). In this scenario, during precession minima, SW monsoon winds were weaker which prevented sufficient cooling of the relatively warm surface waters during this time. Consequently, relatively warm, and less saline waters remained at the surface, creating a strong pycnocline at shallow depths which acted as a pseudo-sea floor and optimum living conditions for taxa such as *Polysphaeridium* (Figure 8). Evidence for this includes high SSTs simultaneous with decreased Ti/Ca values and high abundances of *Polysphaeridium* cpx., *Cleistosphaeridium* spp. and *Apteodinium* sp., indicating warm, stratified surface waters during
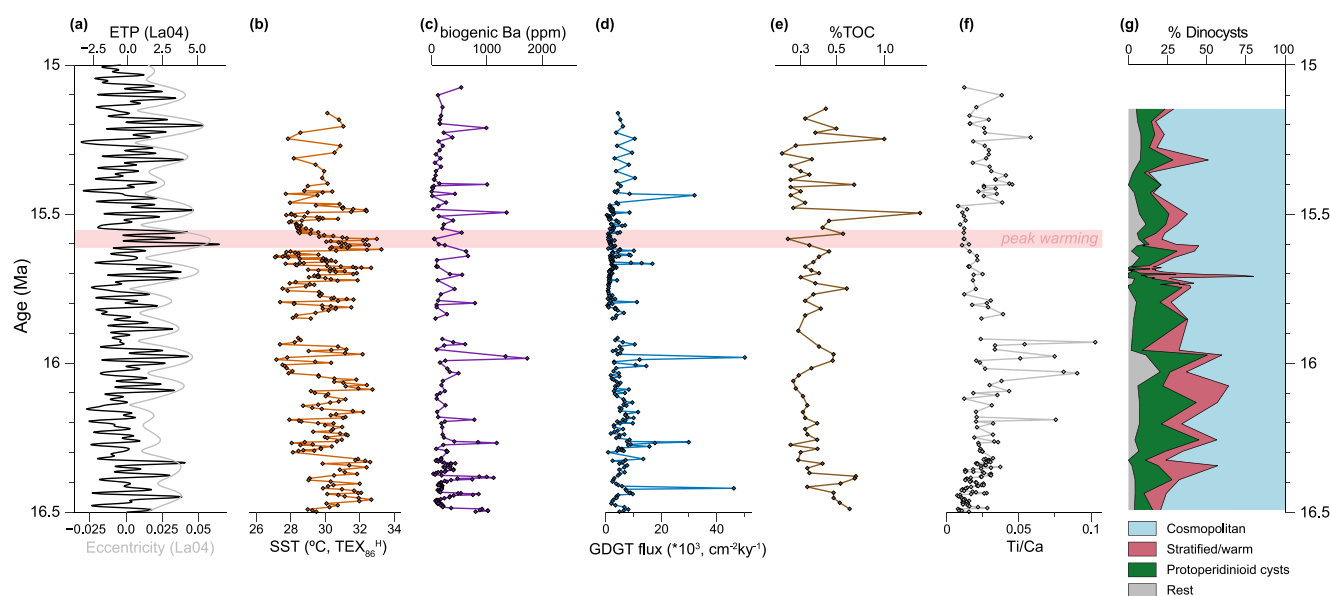
Figure 9. Compilation of geochemical- and palynology proxy records between ~16.5–15.0 Ma at Site 959. (a) Eccentricity, Tilt, Precession (ETP; black) and Eccentricity (gray) from Laskar et al. (2004). (b) TEX_{86}-SST calibrated with exponential calibration TEX_{86}^{H} of Kim et al. (2010). (c) Biogenic barium. (d) TOC-normalized accumulation rate of total GDGTs. (e) %Total Organic Carbon (TOC) plotted on a logarithmic scale. (f) Ti/Ca ratio, indicator for dust supply. (g) areaplot showing relative abundances (%) of major dinocyst groups.

times of decreased WAM intensity. Conversely, during precession maxima intensified NE trade winds facilitate increased offshore surface currents, coastal upwelling, and sufficient mixing of surface waters (Figure 8). Evidently, between ~16.9–16.6 Ma, decreased eccentricity power during a long ~2.4 Myr eccentricity node presented an astronomical configuration that resulted in hyperstratification on ~55 kyr timescales, the combination of precession and obliquity (Spiering et al., 2024). Hyperstratification has also been proposed to account for massive *P. zoharyi* occurrences in the Mediterranean Sea during sapropel formation (Sangiorgi et al., 2006), and at Site 959 during the Middle Eocene Climatic Optimum (Cramwinckel et al., 2019). Furthermore, acmes of the calcareous nannofossil Braarudosphaera in the South Atlantic Ocean during the Oligocene were also related to recurrent hyperstratification episodes during a ~2.4 Myr eccentricity node (Liebrand et al., 2018). Similar to conditions during the MCO at Site 959, a "Monsoon Hypothesis" was proposed in the South Atlantic whereby increased rainfall caused a reduction of surface ocean salinities and mixing, creating a shallow pycnocline (Liebrand et al., 2018). Clearly, careful evaluation of microfossil paleoenvironmental interpretations should be carried out in conjunction with a multi-proxy approach to account for processes such as hyperstratification.

To summarize, we propose that increased WAM intensity following the MCO onset at ~16.9 Ma was caused by warming during the MCO onset relative to the pre-MCO, resulting in increased seasonality. Consequently, the strikingly high amplitude variability in dust influx, SST and export productivity is related to monsoonal winds and resulting coastal upwelling and hyperstratification of the surface waters. Additionally, elevated CO_2 concentrations during the MCO, as evidenced from several proxy studies (Cui et al., 2020; Ji et al., 2018; Sosdian et al., 2018; Steinthorsdottir, Jardine, & Rember, 2021; Stoll et al., 2019; Super et al., 2018), could have been a determining factor in intensifying monsoonal precipitation by increasing the land-ocean surface temperature gradient and enhancing precipitation (Acosta et al., 2022).

5.2.3. Toward the Middle Miocene and MCO Peak Warming

During the younger part of the MCO at Site 959 (~16.5–15.0 Ma), SST shows prominent variability on ~100 kyr eccentricity timescales, while the records of export productivity and dust influx show much less variability on shorter (precession) timescales (Figure 9), in contrast to the astronomical forcing immediately following the MCO onset (~17.0–16.6 Ma). Highest SSTs occur during ~100 and ~400 kyr eccentricity maxima. This suggests the WAM was less sensitive to short or small-scale insolation variations toward the Middle Miocene, which caused less intense and dynamic monsoon circulation over the Gulf of Guinea. Furthermore, dinocyst

assemblages become less diverse and consist of mostly *Spiniferites* spp., *Nematosphaeropsis* spp. and Proto-peridinoid cysts (Figure 9). These taxa are typical for modern surface water assemblages in the Gulf of Guinea, indicating more oceanic conditions with elevated SSTs and nutrient availability (Marret, 1994; Marret et al., 2008).

A decreased WAM in the Middle Miocene, characterized by a smaller monsoon area and weaker circulation compared to the Cenomanian (~95 Ma) and Eocene (~55 Ma), was also suggested from Community Earth System Model simulations by Acosta et al. (2022). Their Miocene simulations, which incorporate a "high ice sheet" and atmospheric CO_2 concentrations of 280 ppm, yielded a monsoon system similar to preindustrial simulations. They ascribed a weakening of the Middle Miocene monsoon to a wider South Atlantic basin compared to during the Eocene and Cenomanian. A narrower Atlantic basin, as well as the Atlantic Ocean protruding into the central African continent due to elevated sea levels, caused increased cross-equatorial con-vection which delivered moisture from the eastern coast of South America to West Africa (Acosta et al., 2022). Moreover, the relatively more northern position of the African continent during the Miocene, relative to the Eocene, shifted monsoon circulation to the subtropics which weakened circulation and increased seasonality (Acosta et al., 2022), although it should be noted that the Miocene simulations were run with modern geography. Relative to the early MCO and intensified WAM at Site 959, we do not find evidence for a change in relative sea-level towards the Middle Miocene and we propose that continental drift was the most important factor deter-mining WAM systematics and intensity.

Similar to dinocyst assemblages immediately following the MCO onset, warm- and inner-neritic to lagoonal taxa show elevated abundances during eccentricity maxima at ~16.4 Ma and ~16 Ma (Figure 9). Temporal resolution of the Site 959 palynological record is insufficient between ~16.5–15.0 Ma to determine whether hyper-stratification on precession timescales caused the periodic occurrence of taxa such as *Polysphaeridium* cpx. Nevertheless, increased WAM variability during eccentricity maxima could have potentially caused hyper-stratification (by modulating precession) when the monsoon was least intense (i.e., weak SW monsoon winds). This eccentricity phasing is apparent from peaks in relative *Polysphaeridium* cpx. abundances during three adjacent ~100 kyr eccentricity maxima between 15.75 and 15.45 Ma.

During the ~400 kyr eccentricity maximum at 15.6 Ma, previously associated with peak warming (Section 5.1), SST shows prominent precession variability. Where temporal resolution in the palynological record allows, specifically between ~15.75 and 15.45 Ma, ~100 kyr eccentricity maxima are associated with increased inner-neritic and lagoonal dinocyst taxa, similar to variability recorded immediately following the MCO onset (~16.9–16.5 Ma). So, even though SST seems sensitive to insolation variation, and thereby WAM dynamics, on pre-cession timescales, conditions such as hyperstratification are seemingly only induced during phases of extreme seasonality through eccentricity modulation of precession. Additionally, increased relative abundances of *Nematosphaeropsis* spp. and Protoperidinoids during relatively low SST alternate with *Polysphaeridium* spp. and other (inner-)neritic taxa, which may imply that *Nematosphaeropsis* spp. thrived during times characterized by increased upwelling of nutrient-rich waters, similar to today. The temporal resolution of Ba_{bio} and Ti/Ca records, however, are too low in this interval to assess this relation.

6. Conclusions

We studied the nearly complete, orbitally tuned Early to Middle Miocene sedimentary record retrieved from ODP Site 959 in the eastern equatorial Atlantic to investigate the tropical climate response across the onset of the MCO and associated dynamics of the WAM. The TEX_{86}-based SST record from ODP Site 959 provides the first, nearly continuous high-resolution tropical temperature record for this time interval and shows SSTs of ~1.5°C warmer compared to the pre-MCO at the onset of the MCO (~16.9 Ma) to average MCO (~17–15 Ma) SSTs of 30°C. SSTs drop by ~1°C at ~16 Ma, likely the result of increased organic carbon burial along continental margins during the Monterey Excursion, acting as a negative carbon cycle feedback. Previously reported peak warming at ~15.6 Ma is not as strongly apparent from SSTs as well as bulk carbonate $\delta^{18}O$ at Site 959 as in deep ocean benthic foraminifer $\delta^{18}O$ records. Therefore, we propose that the deep ocean signal, sourced from high latitudes, was amplified relative to the tropics due to polar amplification.

Our proxy records imply that the WAM system was likely intensified, that is, stronger winds and upwelling, immediately following the MCO onset (~16.9–16.6 Ma). Prior to the MCO (~18.2–17.7 Ma), SST dominantly varies on eccentricity timescales and asymmetrically shaped cycles imply potential influence by high-latitude ice

volume changes. Protoperidinioid dinoflagellate cysts and relatively elevated Ba_{bio} concentrations imply a highly productive surface ocean, likely caused by increased dust influx and upwelling of nutrient-rich waters. Following the MCO onset (~16.9–16.6 Ma), we record anomalously high amplitude variability on precession-to-obliquity timescales in all proxy records. Strikingly high SST amplitude variability at Site 959 (±5°C) is forced by enhanced upwelling and coincides with increased dust supply, paced by a combination tone of precession and obliquity (~50 kyr). Colder and productive conditions alternate with relatively high temperatures and a weaker WAM, that is, weak SW monsoon winds, on 50 kyr timescales. Surprisingly, we record peak absolute concentrations of lagoonal dinocyst taxa *Polysphaeridium* cpx. which we interpret to represent periods of extreme stratification of the surface waters, that is, hyperstratification, caused by diminished vertical mixing of surface waters by weak SW monsoons. Increased *Polysphaeridium* cpx. occurrences during eccentricity maxima in later parts of the MCO (~16.6–15.0 Ma) suggests that hyperstratification occurred on longer timescales, when monsoon intensity was more sensitive to most extreme insolation variations during ~400 kyr eccentricity maxima.

Conflict of Interest

The authors declare no conflicts of interest relevant to this study.

Data Availability Statement

The data presented in this study are available on Zenodo (Sluijs et al., 2023).

References

Acosta, R. P., Ladant, J., Zhu, J., & Poulsen, C. J. (2022). Evolution of the Atlantic intertropical convergence zone, and the South American and African monsoons over the past 95-myr and their impact on the tropical rainforests. *Paleoceanography and Paleoclimatology*, *37*(7). https://doi.org/10.1029/2021PA004383

Adegbie, A. T., Schneider, R. R., Röhl, U., & Wefer, G. (2003). Glacial millennial-scale fluctuations in central African precipitation recorded in terrigenous sediment supply and freshwater signals offshore Cameroon. *Palaeogeography, Palaeoclimatology, Palaeoecology*, *197*(3–4), 323–333. https://doi.org/10.1016/S0031-0182(03)00474-7

Awad, W. K., & Oboh-Ikuenobe, F. E. (2019). Paleogene-early Neogene paleoenvironmental reconstruction based on palynological analysis of ODP Hole 959A, West Africa. *Marine Micropaleontology*, *148*, 29–45. https://doi.org/10.1016/j.marmicro.2019.03.003

Basile, C., Mascle, J., Benkhelil, J., & Bouillin, J. (Eds.). (1998). *Geodynamic evolution of the Côte d'Ivoire-Ghana transform margin: An overview of Leg 159 results* (Vol. 159). Ocean Drilling Program. https://doi.org/10.2973/odp.proc.sr.159.1998

Beddow, H. M., Liebrand, D., Sluijs, A., Wade, B. S., & Lourens, L. J. (2016). Global change across the Oligocene-Miocene transition: High-resolution stable isotope records from IODP Site U1334 (equatorial Pacific Ocean): The OMT at Site U1334. *Paleoceanography*, *31*(1), 81–97. https://doi.org/10.1002/2015PA002820

Berner, R. A. (1982). Burial of organic carbon and pyrite sulfur in the modern ocean; its geochemical and environmental significance. *American Journal of Science*, *282*(4), 451–473. https://doi.org/10.2475/ajs.282.4.451

Berner, R. A., Lasaga, A. C., & Garrels, R. M. (1983). The carbonate-silicate geochemical cycle and its effect on atmospheric carbon dioxide over the past 100 million years. *American Journal of Science*, *283*(7), 641–683. https://doi.org/10.2475/ajs.283.7.641

Blaga, C. I., Reichart, G.-J., Heiri, O., & Sinninghe Damsté, J. S. (2009). Tetraether membrane lipid distributions in water-column particulate matter and sediments: A study of 47 European lakes along a north–south transect. *Journal of Paleolimnology*, *41*(3), 523–540. https://doi.org/10.1007/s10933-008-9242-2

Bosmans, J. H. C., Drijfhout, S. S., Tuenter, E., Hilgen, F. J., Lourens, L. J., & Rohling, E. J. (2015). Precession and obliquity forcing of the freshwater budget over the Mediterranean. *Quaternary Science Reviews*, *123*, 16–30. https://doi.org/10.1016/j.quascirev.2015.06.008

Bosmans, J. H. C., Hilgen, F. J., Tuenter, E., & Lourens, L. J. (2015). Obliquity forcing of low-latitude climate. *Climate of the Past*, *11*(10), 1335–1346. https://doi.org/10.5194/cp-11-1335-2015

Brinkhuis, H., Powell, A. J., Zevenboom, D., Head, M. J., & Wrenn, J. H. (1992). High-resolution dinoflagellate cyst stratigraphy of the Oligocene/Miocene transition interval in northwest and central Italy. In *Neogene and quaternary dinoflagellate cysts and acritarchs* (Vol. 219(258)). American Association of Stratigraphic Palynologists Foundation.

Brinkhuis, H., Sengers, S., Sluijs, A., Warnaar, J., & Williams, G. L. (2003). *Latest cretaceous-earliest Oligocene and quaternary cysts, ODP site 1172, East Tasman Plateau*. (N. F. Exon, J. P. Kennett, & M. J. Malone, Eds.) (Vol. 189). Ocean Drilling Program. https://doi.org/10.2973/odp.proc.sr.189.2004

Brinkhuis, H., & Zachariasse, W. J. (1988). Dinoflagellate cysts, sea level changes and planktonic foraminifers across the Cretaceous-Tertiary boundary at El Haria, northwest Tunisia. *Marine Micropaleontology*, *13*(2), 153–191. https://doi.org/10.1016/0377-8398(88)90002-3

Burke, K. D., Williams, J. W., Chandler, M. A., Haywood, A. M., Lunt, D. J., & Otto-Bliesner, B. L. (2018). Pliocene and Eocene provide best analogs for near-future climates. *Proceedings of the National Academy of Sciences of the United States of America*, *115*(52), 13288–13293. https://doi.org/10.1073/pnas.1809600115

Camberlin, P., Janicot, S., & Poccard, I. (2001). Seasonality and atmospheric dynamics of the teleconnection between African rainfall and tropical sea-surface temperature: Atlantic vs. ENSO. *International Journal of Climatology*, *21*(8), 973–1005. https://doi.org/10.1002/joc.673

Challinor, A., Wheeler, T., Garforth, C., Craufurd, P., & Kassam, A. (2007). Assessing the vulnerability of food crop systems in Africa to climate change. *Climatic Change*, *83*(3), 381–399. https://doi.org/10.1007/s10584-007-9249-0

Collins, M., Knutti, R., Arblaster, J., Dufresne, J.-L., Fichefet, T., Gao, X., et al. (2013). Long-term Climate Change: Projections, Commitments and Irreversibility. In T. F. Stocker, et al. (Eds.), *Climate change 2013: The physical science Basis. Contribution of working group I to the Fifth assessment report of the Intergovernmental Panel on climate change*. Cambridge University Press.

Cramwinckel, M. J., Huber, M., Kocken, I. J., Agnini, C., Bijl, P. K., Bohaty, S. M., et al. (2018). Synchronous tropical and polar temperature evolution in the Eocene. *Nature*, *559*(7714), 382–386. https://doi.org/10.1038/s41586-018-0272-2

Cramwinckel, M. J., van der Ploeg, R., Bijl, P. K., Peterse, F., Bohaty, S. M., Röhl, U., et al. (2019). Harmful algae and export production collapse in the equatorial Atlantic during the zenith of Middle Eocene Climatic Optimum warmth. *Geology*, *47*(3), 247–250. https://doi.org/10.1130/G45614.1

Cui, Y., Schubert, B. A., & Jahren, A. H. (2020). A 23 m.y. record of low atmospheric CO2. *Geology*, *48*(9), 888–892. https://doi.org/10.1130/G47681.1

deMenocal, P. B., Ruddiman, W. F., & Pokras, E. M. (1993). Influences of High- and Low-Latitude Processes on African Terrestrial Climate: Pleistocene Eolian Records from Equatorial Atlantic Ocean Drilling Program Site 663. *Paleoceanography*, *8*(2), 209–242. https://doi.org/10.1029/93PA02688

De Schepper, S., Fischer, E. I., Groeneveld, J., Head, M. J., & Matthiessen, J. (2011). Deciphering the palaeoecology of Late Pliocene and Early Pleistocene dinoflagellate cysts. *Palaeogeography, Palaeoclimatology, Palaeoecology*, *309*(1–2), 17–32. https://doi.org/10.1016/j.palaeo.2011.04.020

Diester-Haass, L., Billups, K., Gröcke, D. R., François, L., Lefebvre, V., & Emeis, K. C. (2009). Mid-Miocene paleoproductivity in the Atlantic Ocean and implications for the global carbon cycle: MID-MIOCENE PALEOPRODUCTIVITY. *Paleoceanography*, *24*(1). https://doi.org/10.1029/2008PA001605

Djakouré, S., Penven, P., Bourlès, B., Koné, V., & Veitch, J. (2017). Respective Roles of the Guinea Current and Local Winds on the Coastal Upwelling in the Northern Gulf of Guinea. *Journal of Physical Oceanography*, *47*(6), 1367–1387. https://doi.org/10.1175/JPO-D-16-0126.1

Dupont, L. M., Marret, F., & Winn, K. (1998). Land-sea correlation by means of terrestrial and marine palynomorphs from the equatorial East Atlantic: Phasing of SE trade winds and the oceanic productivity. *Palaeogeography, Palaeoclimatology, Palaeoecology*, *142*(1–2), 51–84. https://doi.org/10.1016/S0031-0182(97)00146-6

Fensome, R. A. (1993). A classification of living and fossil dinoflagellates. In *Micropaleontology* (Vol. 7, pp. 1–351). Special Publication.

Fox, L. R., Wade, B. S., Holbourn, A., Leng, M. J., & Bhatia, R. (2021). Temperature gradients across the Pacific Ocean during the middle miocene. *Paleoceanography and Paleoclimatology*, *36*(6). https://doi.org/10.1029/2020PA003924

Frieling, J., & Sluijs, A. (2018). Towards quantitative environmental reconstructions from ancient non-analogue microfossil assemblages: Ecological preferences of Paleocene – Eocene dinoflagellates. *Earth-Science Reviews*, *185*, 956–973. https://doi.org/10.1016/j.earscirev.2018.08.014

Gadgil, S. (2018). The monsoon system: Land–sea breeze or the ITCZ? *Journal of Earth System Science*, *127*(1), 1. https://doi.org/10.1007/s12040-017-0916-x

Grimaud, J.-L., Rouby, D., Chardon, D., & Beauvais, A. (2018). Cenozoic sediment budget of West Africa and the Niger delta. *Basin Research*, *30*(2), 169–186. https://doi.org/10.1111/bre.12248

Guitián, J., Phelps, S., Polissar, P. J., Ausín, B., Eglinton, T. I., & Stoll, H. M. (2019). Midlatitude temperature variations in the oligocene to early miocene. *Paleoceanography and Paleoclimatology*, *34*(8), 1328–1343. https://doi.org/10.1029/2019PA003638

Hannah, M. J. (2006). The palynology of ODP site 1165, Prydz Bay, East Antarctica: A record of Miocene glacial advance and retreat. *Palaeogeography, Palaeoclimatology, Palaeoecology*, *231*(1–2), 120–133. https://doi.org/10.1016/j.palaeo.2005.07.029

Harland, R. (1983). Distribution maps of recent dinoflagellate cysts in bottom sediments from the North Atlantic Ocean and adjacent seas. *Palaeontology*, *26*(2), 321–387.

Hartman, J. D., Sangiorgi, F., Salabarnada, A., Peterse, F., Houben, A. J. P., Schouten, S., et al. (2018). Paleoceanography and ice sheet variability offshore Wilkes Land, Antarctica – Part 3: Insights from Oligocene–Miocene TEX$_{86}$-based sea surface temperature reconstructions. *Climate of the Past*, *14*(9), 1275–1297. https://doi.org/10.5194/cp-14-1275-2018

Hedges, J. I., & Keil, R. G. (1995). Sedimentary organic matter preservation: An assessment and speculative synthesis. *Marine Chemistry*, *49*(2), 81–115. https://doi.org/10.1016/0304-4203(95)00008-F

Herbert, T. D., Rose, R., Dybkjær, K., Rasmussen, E. S., & Śliwińska, K. K. (2020). Bihemispheric warming in the Miocene climatic optimum as seen from the Danish North Sea. *Paleoceanography and Paleoclimatology*, *35*(10). https://doi.org/10.1029/2020PA003935

Ho, S. L., & Laepple, T. (2015). Glacial cooling as inferred from marine temperature proxies TEX$_{H}$86 and UK′37. *Earth and Planetary Science Letters*, *409*, 15–22. https://doi.org/10.1016/j.epsl.2014.10.033

Ho, S. L., & Laepple, T. (2016). Flat meridional temperature gradient in the early Eocene in the subsurface rather than surface ocean. *Nature Geoscience*, *9*(8), 606–610. https://doi.org/10.1038/ngeo2763

Hoem, F. S., Sauermilch, I., Hou, S., Brinkhuis, H., Sangiorgi, F., & Bijl, P. K. (2021). Late Eocene–early Miocene evolution of the southern Australian subtropical front: A marine palynological approach. *Journal of Micropalaeontology*, *40*(2), 175–193. https://doi.org/10.5194/jm-40-175-2021

Holbourn, A., Kuhnt, W., Kochhann, K. G. D., Andersen, N., & Sebastian Meier, K. J. (2015). Global perturbation of the carbon cycle at the onset of the Miocene Climatic Optimum. *Geology*, *43*(2), 123–126. https://doi.org/10.1130/G36317.1

Holbourn, A., Kuhnt, W., Schulz, M., Flores, J.-A., & Andersen, N. (2007). Orbitally-paced climate evolution during the middle Miocene "Monterey" carbon-isotope excursion. *Earth and Planetary Science Letters*, *261*(3–4), 534–550. https://doi.org/10.1016/j.epsl.2007.07.026

Holbourn, A., Kuhnt, W., Simo, J. A. T., & Li, Q. (2004). Middle Miocene isotope stratigraphy and paleoceanographic evolution of the northwest and southwest Australian margins (Wombat Plateau and Great Australian Bight). *Palaeogeography, Palaeoclimatology, Palaeoecology*, *208*(1–2), 1–22. https://doi.org/10.1016/j.palaeo.2004.02.003

Hollis, C. J., Dunkley Jones, T., Anagnostou, E., Bijl, P. K., Cramwinckel, M. J., Cui, Y., et al. (2019). The DeepMIP contribution to PMIP4: Methodologies for selection, compilation and analysis of latest Paleocene and early Eocene climate proxy data, incorporating version 0.1 of the DeepMIP database. *Geoscientific Model Development*, *12*(7), 3149–3206. https://doi.org/10.5194/gmd-12-3149-2019

Hopmans, E. C., Schouten, S., & Sinninghe Damsté, J. S. (2016). The effect of improved chromatography on GDGT-based palaeoproxies. *Organic Geochemistry*, *93*, 1–6. https://doi.org/10.1016/j.orggeochem.2015.12.006

Hopmans, E. C., Weijers, J. W. H., Schefuß, E., Herfort, L., Sinninghe Damsté, J. S., & Schouten, S. (2004). A novel proxy for terrestrial organic matter in sediments based on branched and isoprenoid tetraether lipids. *Earth and Planetary Science Letters*, *224*(1–2), 107–116. https://doi.org/10.1016/j.epsl.2004.05.012

Hsu, P., Li, T., Murakami, H., & Kitoh, A. (2013). Future change of the global monsoon revealed from 19 CMIP5 models. *Journal of Geophysical Research: Atmospheres*, *118*(3), 1247–1260. https://doi.org/10.1002/jgrd.50145

Hurley, S. J., Lipp, J. S., Close, H. G., Hinrichs, K.-U., & Pearson, A. (2018). Distribution and export of isoprenoid tetraether lipids in suspended particulate matter from the water column of the Western Atlantic Ocean. *Organic Geochemistry*, *116*, 90–102. https://doi.org/10.1016/j.orggeochem.2017.11.010

Ingalls, A. E., Shah, S. R., Hansman, R. L., Aluwihare, L. I., Santos, G. M., Druffel, E. R. M., & Pearson, A. (2006). Quantifying archaeal community autotrophy in the mesopelagic ocean using natural radiocarbon. *Proceedings of the National Academy of Sciences of the United States of America*, *103*(17), 6442–6447. https://doi.org/10.1073/pnas.0510157103

Jaramillo, C. A., & Oboh-Ikuenobe, F. E. (1999). Sequence stratigraphic interpretations from palynofacies, dinocyst and lithological data of Upper Eocene–Lower Oligocene strata in southern Mississippi and Alabama, U.S. Gulf Coast. *Palaeogeography, Palaeoclimatology, Palaeoecology*, *145*(4), 259–302. https://doi.org/10.1016/S0031-0182(98)00126-6

Ji, S., Nie, J., Lechler, A., Huntington, K. W., Heitmann, E. O., & Breecker, D. O. (2018). A symmetrical CO2 peak and asymmetrical climate change during the middle Miocene. *Earth and Planetary Science Letters*, *499*, 134–144. https://doi.org/10.1016/j.epsl.2018.07.011

Kim, J.-H., Schouten, S., Rodrigo-Gámiz, M., Rampen, S., Marino, G., Huguet, C., et al. (2015). Influence of deep-water derived isoprenoid tetraether lipids on the TEX 86 H paleothermometer in the Mediterranean Sea. *Geochimica et Cosmochimica Acta*, *150*, 125–141. https://doi.org/10.1016/j.gca.2014.11.017

Kim, J.-H., van der Meer, J., Schouten, S., Helmke, P., Willmott, V., Sangiorgi, F., et al. (2010). New indices and calibrations derived from the distribution of crenarchaeal isoprenoid tetraether lipids: Implications for past sea surface temperature reconstructions. *Geochimica et Cosmochimica Acta*, *74*(16), 4639–4654. https://doi.org/10.1016/j.gca.2010.05.027

Kochhann, K. G. D., Holbourn, A., Kuhnt, W., & Xu, J. (2017). Eastern equatorial Pacific benthic foraminiferal distribution and deep water temperature changes during the early to middle Miocene. *Marine Micropaleontology*, *133*, 28–39. https://doi.org/10.1016/j.marmicro.2017.05.002

Kocken, I. J., Cramwinckel, M. J., Zeebe, R. E., Middelburg, J. J., & Sluijs, A. (2019). The 405 kyr and 2.4 Myr eccentricity components in Cenozoic carbon isotope records. *Climate of the Past*, *15*(1), 91–104. https://doi.org/10.5194/cp-15-91-2019

Köthe, A. (1990). Paleogene Dinoflagellates from Northwest Germany - Biostratigraphy and Paleoenvironments.

Kutzbach, J. E., Chen, G., Cheng, H., Edwards, R. L., & Liu, Z. (2014). Potential role of winter rainfall in explaining increased moisture in the Mediterranean and Middle East during periods of maximum orbitally-forced insolation seasonality. *Climate Dynamics*, *42*(3), 1079–1095. https://doi.org/10.1007/s00382-013-1692-1

Larrasoaña, J. C., Roberts, A. P., & Rohling, E. J. (2013). Dynamics of green Sahara periods and their role in hominin evolution. *PLoS One*, *8*(10), e76514. https://doi.org/10.1371/journal.pone.0076514

Larrasoaña, J. C., Roberts, A. P., Rohling, E. J., Winklhofer, M., & Wehausen, R. (2003). Three million years of monsoon variability over the northern Sahara. *Climate Dynamics*, *21*(7), 689–698. https://doi.org/10.1007/s00382-003-0355-z

Laskar, J., Robutel, P., Joutel, F., Gastineau, M., Correia, A. C., & Levrard, B. (2004). A long-term numerical solution for the insolation quantities of the Earth. *Astronomy & Astrophysics*, *428*(1), 261–285. https://doi.org/10.1051/0004-6361:20041335

Lear, C. H., Mawbey, E. M., & Rosenthal, Y. (2010). Cenozoic benthic foraminiferal Mg/Ca and Li/Ca records: Toward unlocking temperatures and saturation states: Ocean temperatures and saturation state. *Paleoceanography*, *25*(4). https://doi.org/10.1029/2009PA001880

Lengger, S. K., Hopmans, E. C., Sinninghe Damsté, J. S., & Schouten, S. (2014). Impact of sedimentary degradation and deep water column production on GDGT abundance and distribution in surface sediments in the Arabian Sea: Implications for the TEX86 paleothermometer. *Geochimica et Cosmochimica Acta*, *142*, 386–399. https://doi.org/10.1016/j.gca.2014.07.013

Leutert, T. J., Auderset, A., Martínez-García, A., Modestou, S., & Meckler, A. N. (2020). Coupled Southern Ocean cooling and Antarctic ice sheet expansion during the middle Miocene. *Nature Geoscience*, *13*(9), 634–639. https://doi.org/10.1038/s41561-020-0623-0

Levy, R., Harwood, D., Florindo, F., Sangiorgi, F., Tripati, R., von Eynatten, H., et al. (2016). Antarctic ice sheet sensitivity to atmospheric CO$_2$ variations in the early to mid-Miocene. *Proceedings of the National Academy of Sciences*, *113*(13), 3453–3458. https://doi.org/10.1073/pnas.1516030113

Liebrand, D., Beddow, H. M., Lourens, L. J., Pälike, H., Raffi, I., Bohaty, S. M., et al. (2016). Cyclostratigraphy and eccentricity tuning of the early Oligocene through early Miocene (30.1–17.1 Ma): Cibicides mundulus stable oxygen and carbon isotope records from Walvis Ridge Site 1264. *Earth and Planetary Science Letters*, *450*, 392–405. https://doi.org/10.1016/j.epsl.2016.06.007

Liebrand, D., de Bakker, A. T. M., Beddow, H. M., Wilson, P. A., Bohaty, S. M., Ruessink, G., et al. (2017). Evolution of the early Antarctic ice ages. *Proceedings of the National Academy of Sciences of the United States of America*, *114*(15), 3867–3872. https://doi.org/10.1073/pnas.1615440114

Liebrand, D., Raffi, I., Fraguas, Á., Laxenaire, R., Bosmans, J. H. C., Hilgen, F. J., et al. (2018). Orbitally Forced Hyperstratification of the Oligocene South Atlantic Ocean. *Paleoceanography and Paleoclimatology*, *33*(5), 511–529. https://doi.org/10.1002/2017PA003222

Liu, Z., Pagani, M., Zinniker, D., DeConto, R., Huber, M., Brinkhuis, H., et al. (2009). Global cooling during the Eocene-Oligocene climate transition. *Science*, *323*(5918), 1187–1190. https://doi.org/10.1126/science.1166368

Locarnini, R. A., Mishonov, A. V., Antonov, J. I., Boyer, T. P., Garcia, H. E., Baranova, O. K., et al. (2013). World ocean atlas 2013. *Temperature*, *1*. https://doi.org/10.7289/V55X26VD

Louwye, S., De Schepper, S., Laga, P., & Vandenberghe, N. (2007). The Upper Miocene of the southern North Sea Basin (northern Belgium): A palaeoenvironmental and stratigraphical reconstruction using dinoflagellate cysts. *Geological Magazine*, *144*(1), 33–52. https://doi.org/10.1017/S0016756806002627

Ma, W., Tian, J., Li, Q., & Wang, P. (2011). Simulation of long eccentricity (400-kyr) cycle in ocean carbon reservoir during Miocene Climate Optimum: Weathering and nutrient response to orbital change: THE 400-kyr CYCLE OF OCEANIC δ^{13} C. *Geophysical Research Letters*, *38*(10). https://doi.org/10.1029/2011GL047680

Marret, F. (1994). Distribution of dinoflagellate cysts in recent marine sediments from the east Equatorial Atlantic (Gulf of Guinea). *Review of Palaeobotany and Palynology*, *84*(1), 1–22. https://doi.org/10.1016/0034-6667(94)90038-8

Marret, F., Bradley, L., de Vernal, A., Hardy, W., Kim, S.-Y., Mudie, P., et al. (2020). From bi-polar to regional distribution of modern dino-flagellate cysts, an overview of their biogeography. *Marine Micropaleontology*, *159*, 101753. https://doi.org/10.1016/j.marmicro.2019.101753

Marret, F., Scourse, J., Kennedy, H., Ufkes, E., & Jansen, J. H. F. (2008). Marine production in the Congo-influenced SE Atlantic over the past 30,000 years: A novel dinoflagellate-cyst based transfer function approach. *Marine Micropaleontology*, *68*(1–2), 198–222. https://doi.org/10.1016/j.marmicro.2008.01.004

Marzocchi, A., Lunt, D. J., Flecker, R., Bradshaw, C. D., Farnsworth, A., & Hilgen, F. J. (2015). Orbital control on late Miocene climate and the North African monsoon: Insight from an ensemble of sub-precessional simulations. *Climate of the Past*, *11*(10), 1271–1295. https://doi.org/10.5194/cp-11-1271-2015

Mascle, J. (1996). Pre-Cruise and Site Surveys: A Synthesis of Marine Geological and Geophysical Data on the Cote D'ivoire-Ghana Transform Margin. In C. Basile, J. Mascle, F. Sage, G. Lamarche, & B. Pontoise (Eds.), *Proceedings of the Ocean Drilling Program, 159 initial reports* (Vol. 159). Ocean Drilling Program. https://doi.org/10.2973/odp.proc.ir.159.103.1996

Mascle, J., Lohmann, G. P., & Clift, P. D., & Shipboard Scientific Party. (1996). Proceedings of the Ocean Drilling Program, 159 initial reports. In *SITE 959* (Vol. 159). Ocean Drilling Program. https://doi.org/10.2973/odp.proc.ir.159.1996

Masson-Delmotte, V., Zhai, P., Pirani, A., Connors, S. L., Péan, C., Berger, S., et al. (2021). IPCC 2021, Summary for Policymakers. In *Climate change 2021: The physical science basis. Contribution of working group I to the sixth assessment report of the intergovernmental panel on climate change* (pp. 3–32). Cambridge University Press. https://doi.org/10.1017/9781009157896.001

Miller, K., Browning, J., Schmelz, W. J., Kopp, R., Mountain, G., & Wright, J. (2020). Cenozoic sea-level and cryospheric evolution from deep-sea geochemical and continental margin records (other). Display. https://doi.org/10.5194/egusphere-egu2020-10017

Modestou, S. E., Leutert, T. J., Fernandez, A., Lear, C. H., & Meckler, A. N. (2020). Warm Middle Miocene Indian Ocean Bottom Water Temperatures: Comparison of Clumped Isotope and Mg/Ca-Based Estimates. *Paleoceanography and Paleoclimatology*, *35*(11). https://doi.org/10.1029/2020PA003927

Norris, R. D. (1998). Miocene–Pliocene surface-water hydrography of the eastern equatorial Atlantic. *Ocean Drilling Program*, *159*. https://doi.org/10.2973/odp.proc.sr.159.1998

Oboh-Ikuenobe, F. E., Hoffmeister, A. P., & Chrisfield, R. A. (1999). Cyclical distribution of dispersed organic matter and dinocysts, ODP site 959 (early Oligocene-early Miocene, côte d' Ivoire-Ghana transform margin). *Palynology*, *23*(1), 87–96. https://doi.org/10.1080/01916122.1999.9989523

O'Brien, C. L., Robinson, S. A., Pancost, R. D., Sinninghe Damsté, J. S., Schouten, S., Lunt, D. J., et al. (2017). Cretaceous sea-surface temperature evolution: Constraints from TEX86 and planktonic foraminiferal oxygen isotopes. *Earth-Science Reviews*, *172*, 224–247. https://doi.org/10.1016/j.earscirev.2017.07.012

Oksanen, J., Simpson, G. L., Blanchet, F. G., Kindt, R., Legendre, P., Minchin, P. R., et al. (2022). Package "vegan" (Version R package version 2.6-4). Retrieved from https://CRAN.R-project.org/package=vegan

Pross, J., & Brinkhuis, H. (2005). Organic-walled dinoflagellate cysts as paleoenvironmental indicators in the Paleogene; a synopsis of concepts. *Paläontologische Zeitschrift*, *79*(1), 53–59. https://doi.org/10.1007/BF03021753

Quaijtaal, W., Donders, T. H., Persico, D., & Louwye, S. (2014). Characterising the middle Miocene Mi-events in the Eastern North Atlantic realm: A first high-resolution marine palynological record from the Porcupine Basin. *Palaeogeography, Palaeoclimatology, Palaeoecology*, *399*, 140–159. https://doi.org/10.1016/j.palaeo.2014.02.017

Rattanasriampaipong, R., Zhang, Y. G., Pearson, A., Hedlund, B. P., & Zhang, S. (2022). Archaeal lipids trace ecology and evolution of marine ammonia-oxidizing archaea. *Proceedings of the National Academy of Sciences of the United States of America*, *119*(31), e2123193119. https://doi.org/10.1073/pnas.2123193119

Reichart, G.-J., Brinkhuis, H., Huiskamp, F., & Zachariasse, W. J. (2004). Hyperstratification following glacial overturning events in the northern Arabian Sea. *Paleoceanography*, *19*(2). https://doi.org/10.1029/2003PA000900

Rohling, E. J., Foster, G. L., Gernon, T. M., Grant, K. M., Heslop, D., Hibbert, F. D., et al. (2022). Comparison and synthesis of sea-level and deep-sea temperature variations over the past 40 million years. *Reviews of Geophysics*, *60*(4), e2022RG000775. https://doi.org/10.1029/2022RG000775

Rossignol-Strick, M. (1985). Mediterranean Quaternary sapropels, an immediate response of the African monsoon to variation of insolation. *Palaeogeography, Palaeoclimatology, Palaeoecology*, *49*(3), 237–263. https://doi.org/10.1016/0031-0182(85)90056-2

Rousselle, G., Beltran, C., Sicre, M.-A., Raffi, I., & De Rafélis, M. (2013). Changes in sea-surface conditions in the Equatorial Pacific during the middle Miocene–Pliocene as inferred from coccolith geochemistry. *Earth and Planetary Science Letters*, *361*, 412–421. https://doi.org/10.1016/j.epsl.2012.11.003

Sangiorgi, F., Bijl, P. K., Passchier, S., Salzmann, U., Schouten, S., McKay, R., et al. (2018). Southern Ocean warming and Wilkes Land ice sheet retreat during the mid-Miocene. *Nature Communications*, *9*(1), 317. https://doi.org/10.1038/s41467-017-02609-7

Sangiorgi, F., Dinelli, E., Maffioli, P., Capotondi, L., Giunta, S., Morigi, C., et al. (2006). Geochemical and micropaleontological characterisation of a Mediterranean sapropel S5: A case study from core BAN89GC09 (south of Crete). *Palaeogeography, Palaeoclimatology, Palaeoecology*, *235*(1), 192–207. https://doi.org/10.1016/j.palaeo.2005.09.029

Sangiorgi, F., Quaijtaal, W., Donders, T. H., Schouten, S., & Louwye, S. (2021). Middle Miocene Temperature and Productivity Evolution at a Northeast Atlantic Shelf Site (IODP U1318, Porcupine Basin): Global and Regional Changes. *Paleoceanography and Paleoclimatology*, *36*(7). https://doi.org/10.1029/2020PA004059

Schouten, S., Hopmans, E. C., Schefuß, E., & Sinninghe Damsté, J. S. (2002). Distributional variations in marine crenarchaeotal membrane lipids: A new tool for reconstructing ancient sea water temperatures? *Earth and Planetary Science Letters*, *204*(1–2), 265–274. https://doi.org/10.1016/S0012-821X(02)00979-2

Schouten, S., Hopmans, E. C., & Sinninghe Damsté, J. S. (2013). The organic geochemistry of glycerol dialkyl glycerol tetraether lipids: A review. *Organic Geochemistry*, *54*, 19–61. https://doi.org/10.1016/j.orggeochem.2012.09.006

Schreck, M., & Matthiessen, J. (2013). Batiacasphaera micropapillata: Palaeobiogeographic distribution and palaeoecological implications of a critical Neogene species complex. In *Biological and geological perspectives of dinoflagellates* (p. 15). The Micropalaeontological Society, Special Publications.

Schreck, M., Nam, S.-I., Clotten, C., Fahl, K., De Schepper, S., Forwick, M., & Matthiessen, J. (2017). Neogene dinoflagellate cysts and acritarchs from the high northern latitudes and their relation to sea surface temperature. *Marine Micropaleontology*, *136*, 51–65. https://doi.org/10.1016/j.marmicro.2017.09.003

Seth, A., Giannini, A., Rojas, M., Rauscher, S. A., Bordoni, S., Singh, D., & Camargo, S. J. (2019). Monsoon Responses to Climate Changes—Connecting Past, Present and Future. *Current Climate Change Reports*, *5*(2), 63–79. https://doi.org/10.1007/s40641-019-00125-y

Shah, S. R., Mollenhauer, G., Ohkouchi, N., Eglinton, T. I., & Pearson, A. (2008). Origins of archaeal tetraether lipids in sediments: Insights from radiocarbon analysis. *Geochimica et Cosmochimica Acta*, *72*(18), 4577–4594. https://doi.org/10.1016/j.gca.2008.06.021

Sluijs, A., Fokkema, C. D., Agterhuis, T., Gerritsma, D., de Goeij, M., Liu, X., et al. (2023). Ocean Drilling Program Site 959 Datasets (1.0.0) [Dataset]. *Zenodo*. https://doi.org/10.5281/zenodo.8309643

Sluijs, A., Pross, J., & Brinkhuis, H. (2005). From greenhouse to icehouse; organic-walled dinoflagellate cysts as paleoenvironmental indicators in the Paleogene. *Earth-Science Reviews*, *68*(3–4), 281–315. https://doi.org/10.1016/j.earscirev.2004.06.001

Sosdian, S., Coxall, H., Steinthorsdottir, M., & Lawrence, K. (2024). Miocene temperature portal. Dataset version 3. *Bolin Centre Database*. https://doi.org/10.17043/miocene-temperature-portal-3

Sosdian, S. M., Babila, T. L., Greenop, R., Foster, G. L., & Lear, C. H. (2020). Ocean Carbon Storage across the middle Miocene: A new interpretation for the Monterey Event. *Nature Communications*, *11*(1), 134. https://doi.org/10.1038/s41467-019-13792-0

Sosdian, S. M., Greenop, R., Hain, M. P., Foster, G. L., Pearson, P. N., & Lear, C. H. (2018). Constraining the evolution of Neogene ocean carbonate chemistry using the boron isotope pH proxy. *Earth and Planetary Science Letters*, *498*, 362–376. https://doi.org/10.1016/j.epsl.2018.06.017

Sosdian, S. M., & Lear, C. H. (2020). Initiation of the Western Pacific Warm Pool at the Middle Miocene Climate Transition? *Paleoceanography and Paleoclimatology*, *35*(12). https://doi.org/10.1029/2020PA003920

Spiering, B. R., Wubben, E., Hilgen, F. J., & Sluijs, A. (2024). Early to Middle Miocene astronomically-paced climate dynamics in the eastern equatorial Atlantic. *Paleoceanography & Paleoclimatology*, *39*, e2023PA004768. https://doi.org/10.1029/2023PA004768

Steinthorsdottir, M., Coxall, H. K., de Boer, A. M., Huber, M., Barbolini, N., Bradshaw, C. D., et al. (2021). The Miocene: The future of the past. *Paleoceanography and Paleoclimatology*, *36*(4). https://doi.org/10.1029/2020PA004037

Steinthorsdottir, M., Jardine, P. E., & Rember, W. C. (2021). Near-Future pCO_2 During the Hot Miocene Climatic Optimum. *Paleoceanography and Paleoclimatology*, *36*(1). https://doi.org/10.1029/2020PA003900

Stoll, H. M., Guitian, J., Hernandez-Almeida, I., Mejia, L. M., Phelps, S., Polissar, P., et al. (2019). Upregulation of phytoplankton carbon concentrating mechanisms during low CO2 glacial periods and implications for the phytoplankton pCO2 proxy. *Quaternary Science Reviews*, *208*, 1–20. https://doi.org/10.1016/j.quascirev.2019.01.012

Stramma, L., & England, M. (1999). On the water masses and mean circulation of the South Atlantic Ocean. *Journal of Geophysical Research*, *104*(C9), 20863–20883. https://doi.org/10.1029/1999JC900139

Super, J. R., Thomas, E., Pagani, M., Huber, M., O'Brien, C., & Hull, P. M. (2018). North Atlantic temperature and pCO2 coupling in the early-middle Miocene. *Geology*, *46*(6), 519–522. https://doi.org/10.1130/G40228.1

Super, J. R., Thomas, E., Pagani, M., Huber, M., O'Brien, C. L., & Hull, P. M. (2020). Miocene Evolution of North Atlantic Sea Surface Temperature. *Paleoceanography and Paleoclimatology*, *35*(5). https://doi.org/10.1029/2019PA003748

Taylor, K. W. R., Huber, M., Hollis, C. J., Hernandez-Sanchez, M. T., & Pancost, R. D. (2013). Re-evaluating modern and Palaeogene GDGT distributions: Implications for SST reconstructions. *Global and Planetary Change*, *108*, 158–174. https://doi.org/10.1016/j.gloplacha.2013.06.011

Tiedemann, R., Sarnthein, M., & Shackleton, N. J. (1994). Astronomic timescale for the Pliocene Atlantic d18O and dust flux records of Ocean Drilling program site 659. *Paleoceanography*, *9*(4), 619–638. https://doi.org/10.1126/science.1126255

Tierney, J. E., & Tingley, M. P. (2014). A Bayesian, spatially-varying calibration model for the TEX86 proxy. *Geochimica et Cosmochimica Acta*, *127*, 83–106. https://doi.org/10.1016/j.gca.2013.11.026

Tjallingii, R., Claussen, M., Stuut, J.-B. W., Fohlmeister, J., Jahn, A., Bickert, T., et al. (2008). Coherent high- and low-latitude control of the northwest African hydrological balance. *Nature Geoscience*, *1*(10), 670–675. https://doi.org/10.1038/ngeo289

Torsvik, T. H., Van der Voo, R., Preeden, U., Mac Niocaill, C., Steinberger, B., Doubrovine, P. V., et al. (2012). Phanerozoic polar wander, palaeogeography and dynamics. *Earth-Science Reviews*, *114*(3), 325–368. https://doi.org/10.1016/j.earscirev.2012.06.007

Trauth, M. H., Larrasoaña, J. C., & Mudelsee, M. (2009). Trends, rhythms and events in Plio-Pleistocene African climate. *Quaternary Science Reviews*, *28*(5–6), 399–411. https://doi.org/10.1016/j.quascirev.2008.11.003

Vallé, F., Westerhold, T., & Dupont, L. M. (2017). Orbital-driven environmental changes recorded at ODP Site 959 (eastern equatorial Atlantic) from the Late Miocene to the Early Pleistocene. *International Journal of Earth Sciences*, *106*(3), 1161–1174. https://doi.org/10.1007/s00531-016-1350-z

van der Weijst, C. M. H., van der Laan, K. J., Peterse, F., Reichart, G.-J., Sangiorgi, F., Schouten, S., et al. (2022). A 15-million-year surface- and subsurface-integrated TEX $_{86}$ temperature record from the eastern equatorial Atlantic. *Climate of the Past*, *18*(8), 1947–1962. https://doi.org/10.5194/cp-18-1947-2022

van Hinsbergen, D. J. J., de Groot, L. V., van Schaik, S. J., Spakman, W., Bijl, P. K., Sluijs, A., et al. (2015). A Paleolatitude Calculator for Paleoclimate Studies. *PLoS One*, *10*(6), e0126946. https://doi.org/10.1371/journal.pone.0126946

Varma, D., Hättig, K., van der Meer, M. T. J., Reichart, G.-J., & Schouten, S. (2023). Constraining water depth influence on organic paleo-temperature proxies using sedimentary archives. *Paleoceanography and Paleoclimatology*, *38*(6), e2022PA004533. https://doi.org/10.1029/2022PA004533

Verstraete, J.-M. (1992). The seasonal upwellings in the Gulf of Guinea. *Progress in Oceanography*, *29*(1), 1–60. https://doi.org/10.1016/0079-6611(92)90002-H

Vincent, E., & Berger, W. H. (1985). Carbon dioxide and polar cooling in the Miocene: The Monterey Hypothesis. In E. T. Sundquist & W. S. Broecker (Eds.), *Geophysical monograph series* (pp. 455–468). American Geophysical Union. https://doi.org/10.1029/GM032p0455

Wagner, T. (1998). 41. Pliocene–Pleistocene deposition of carbonate and organic carbon at site 959: Paleoenvironmental implications for the eastern equatorial Atlantic off the ivory coast/Ghana (Vol. *159*). https://doi.org/10.2973/odp.proc.sr.159.1998

Wagner, T. (2002). Late Cretaceous to early Quaternary organic sedimentation in the eastern Equatorial Atlantic. *Palaeogeography, Palaeoclimatology, Palaeoecology*, *179*(1–2), 113–147. https://doi.org/10.1016/S0031-0182(01)00415-1

Wall, D., Dale, B., Lohmann, G. P., & Smith, W. K. (1977). The environmental and climatic distribution of dinoflagellate cysts in modern marine sediments from regions in the North and South Atlantic Oceans and adjacent seas. *Marine Micropaleontology*, *2*, 121–200. https://doi.org/10.1016/0377-8398(77)90008-1

Weijers, J. W. H., Lim, K. L. H., Aquilina, A., Sinninghe Damsté, J. S., & Pancost, R. D. (2011). Biogeochemical controls on glycerol dialkyl glycerol tetraether lipid distributions in sediments characterized by diffusive methane flux: TEX $_{86}$ in sulfate-methane transition zone. *Geochemistry, Geophysics, Geosystems*, *12*(10). https://doi.org/10.1029/2011GC003724

Weijers, J. W. H., Schouten, S., Spaargaren, O. C., & Sinninghe Damsté, J. S. (2006). Occurrence and distribution of tetraether membrane lipids in soils: Implications for the use of the TEX86 proxy and the BIT index. *Organic Geochemistry*, *37*(12), 1680–1693. https://doi.org/10.1016/j.orggeochem.2006.07.018

Weldeab, S., Lea, D. W., Schneider, R. R., & Andersen, N. (2007). 155,000 years of West African Monsoon and Ocean Thermal Evolution. *Science*, *316*(5829), 1303–1307. https://doi.org/10.1126/science.1140461

Westerhold, T., Marwan, N., Drury, A. J., Liebrand, D., Agnini, C., Anagnostou, E., et al. (2020). An astronomically dated record of Earth's climate and its predictability over the last 66 million years. *Science*, *369*(6509), 1383–1387. https://doi.org/10.1126/science.aba6853

Williams, G. L., Fensome, R. A., & MacRae, R. A. (2017). *The Lentin and Williams index of Fossil dinoflagellates 2017 edition*. American Association of Stratigraphic Palynologists foundation.

Woodruff, F., & Savin, S. (1991). Mid-Miocene isotope stratigraphy in the deep sea: High-resolution correlations, paleoclimatic cycles, and sediment preservation. *Paleoceanography*, *6*(6), 755–806. https://doi.org/10.1029/91PA02561

Wubben, E., Veenstra, T., Witkowski, J., Raffi, I., Hilgen, F., Bos, R., et al. (2023). Astrochronology of the Miocene Climatic Optimum record from Ocean Drilling Program Site 959 in the eastern equatorial Atlantic. *Newsletters on Stratigraphy*, *56*(4), 457–484. https://doi.org/10.1127/nos/2023/0749

Zammit, R., Lear, C. H., Samankassou, E., Lourens, L. J., Micallef, A., Pearson, P. N., & Bialik, O. M. (2022). Early Miocene intensification of the North African hydrological cycle: Multi-proxy evidence from the shelf carbonates of Malta. *Paleoceanography and Paleoclimatology*, *37*(9). https://doi.org/10.1029/2022PA004414

Zevenboom, D., Brinkhuis, H., & Visscher, H. (1994). Dinoflagellate cysts palaeoenvironmental analysis of the Oligocene/Miocene transition in northwest and central Italy. *Giornale di Geologia*, *56*, 155–169.

Zhang, Y. G., Pagani, M., & Wang, Z. (2016). Ring Index: A new strategy to evaluate the integrity of TEX$_{86}$ paleothermometry. *Paleoceanography*, *31*(2), 220–232. https://doi.org/10.1002/2015PA002848

Zhang, Y. G., Zhang, C. L., Liu, X.-L., Li, L., Hinrichs, K.-U., & Noakes, J. E. (2011). Methane Index: A tetraether archaeal lipid biomarker indicator for detecting the instability of marine gas hydrates. *Earth and Planetary Science Letters*, *307*(3–4), 525–534. https://doi.org/10.1016/j.epsl.2011.05.031

Zhang, Z., Nisancioglu, K. H., Chandler, M. A., Haywood, A. M., Otto-Bliesner, B. L., Ramstein, G., et al. (2013). Mid-pliocene Atlantic Meridional Overturning Circulation not unlike modern. *Climate of the Past*, *9*(4), 1495–1504. https://doi.org/10.5194/cp-9-1495-2013

Zhang, Z., Ramstein, G., Schuster, M., Li, C., Contoux, C., & Yan, Q. (2014). Aridification of the Sahara desert caused by Tethys Sea shrinkage during the Late Miocene. *Nature*, *513*(7518), 401–404. https://doi.org/10.1038/nature13705

Zonneveld, K. A. F., Chen, L., Möbius, J., & Mahmoud, M. S. (2009). Environmental significance of dinoflagellate cysts from the proximal part of the Po-river discharge plume (off southern Italy, Eastern Mediterranean). *Journal of Sea Research*, *62*(4), 189–213. https://doi.org/10.1016/j.seares.2009.02.003

Zonneveld, K. A. F., Marret, F., Versteegh, G. J. M., Bogus, K., Bonnet, S., Bouimetarhan, I., et al. (2013). Atlas of modern dinoflagellate cyst distribution based on 2405 data points. *Review of Palaeobotany and Palynology*, *191*, 1–197. https://doi.org/10.1016/j.revpalbo.2012.08.003

Zonneveld, K. A. F., Versteegh, G. J. M., & de Lange, G. J. (1997). Preservation of organic-walled dinoflagellate cysts in different oxygen regimes: A 10,000 year natural experiment. *Marine Micropaleontology*, *29*(3–4), 393–405. https://doi.org/10.1016/S0377-8398(96)00032-1